UNIVERSITY OF GOTHENBURG

DEPARTMENT OF PHYSICS

Laser Photodetachment Threshold Spectroscopy
on O^-, Ag^-, PdO^- and AgO^-

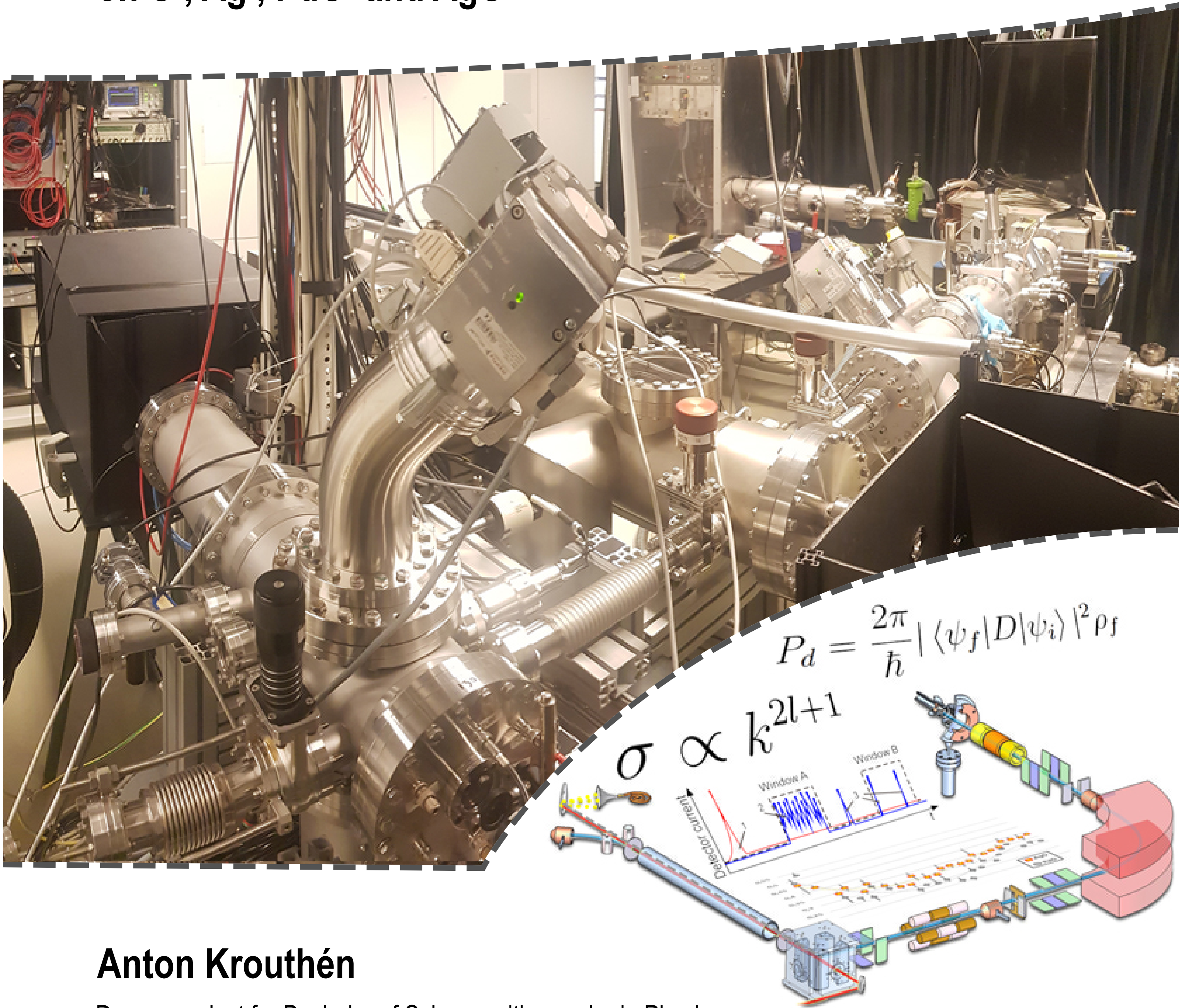

Anton Krouthén

Degree project for Bachelor of Science with a major in Physics
2020, 180HEC

Laser Photodetachment Threshold Spectroscopy on O^-, Ag^-, PdO^- and AgO^-

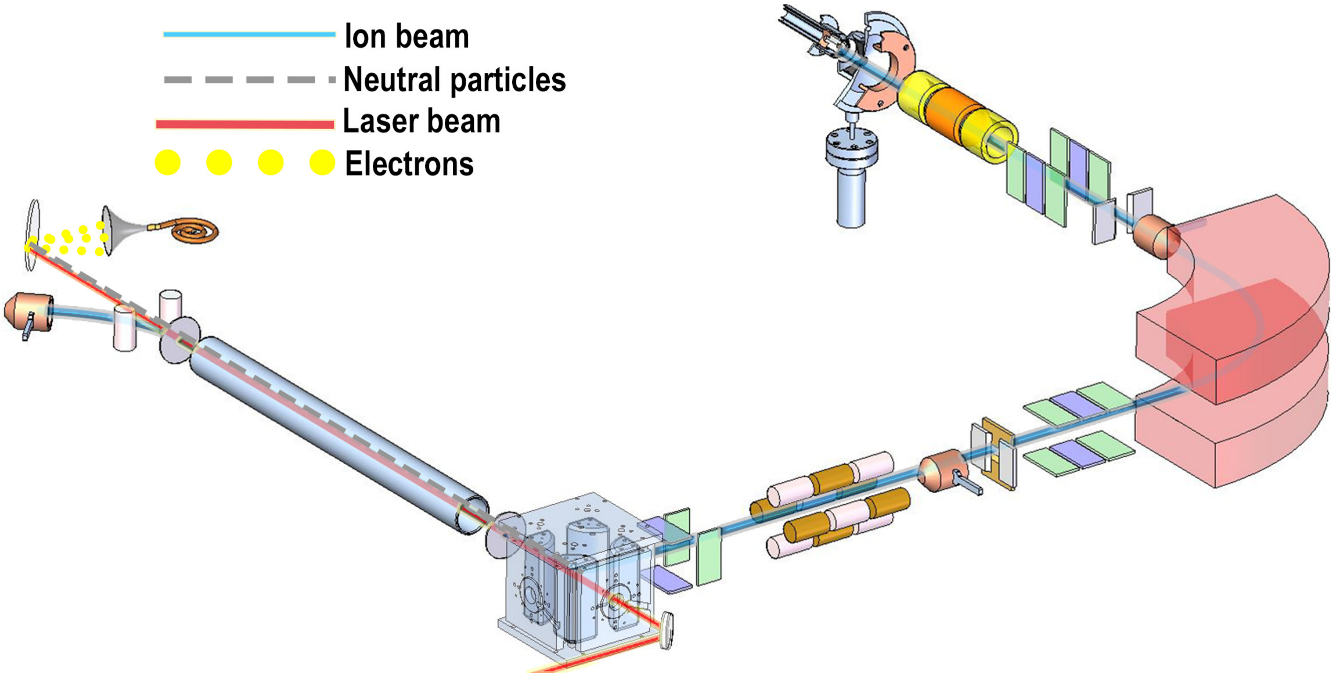

GÖTEBORGS
UNIVERSITET

Laser Photodetachment Threshold Spectroscopy on O^-, Ag^-, PdO^- and AgO^-

Supervisor: Dag Hanstorp
Examinator: Martina Ahlberg

Bachelor thesis 2020
Department of Physics
University of Gothenburg
SE-412 96 Gothenburg
Telephone +46 31 786 1000

Abstract

The aim of this thesis is to investigate the possibility of using anionic oxides in selective laser photodetachment suppression of ^{107}Ag in Accelerator Mass Spectrometry (AMS) studies of ^{107}Pd. The thesis will also give a brief theoretical introduction to negative ions, some general information about AMS and the connection to radiometric dating, and an overview description of Gotheburg University Negative Ion Laser LAboratory (GUNILLA).

Laser Photodetachment Threshold Spectroscopy (LPTS) was performed on O^-, Ag^-, PdO^- and AgO^- to compare the photodetachment cross section behaviours of the anionic silver and palladium oxides and see if you at some laser wavelength can neutralize AgO^- while keeping PdO^- negatively charged. The results show that the photodetachment cross section of PdO^- relatively tightly follows that of AgO^- in the investigated laser wavelenght interval [900 nm - 700 nm] making it impossible to only detach electrons from AgO^-. The conclusion drawn from this is that AgO^- and PdO^- are not suitable molecular candidates for selective laser photodetachment suppression of ^{107}Ag in AMS studies of ^{107}Pd.

The project, though having negative results in the sense of not finding a molecular system fulfilling the properties sought in the AMS application, are not considered unsuccessful. The project experiments are seen as a necessary and successfully investigated stepping stone in the search for an easily created molecular system making selective laser photodetachment suppression of ^{107}Ag in AMS studies of ^{107}Pd possible. The proposed next step is to investigate the photodetachment cross section behaviours of silver and palladium dioxides and fluorides.

Contents

1 Preface

When looking for a thesis project my primary goal was to find something experimental that was not only interesting but also diverse and educative. The AgO^-/PdO^- laser photodetachment threshold spectroscopy project turned out to be that educative experimental process focusing on a theoretical interesting subject with exciting possible applications. This opened up for a rewarding literature study which not only gave me insights into the specific details around the project, but also opened up for a stimulating dive into the world of accelerator mass spectrometry.

Working on the experimental part of the project you touched on a broad range of different physics subjects. The focus on everything from laser physics and particle interactions to quantum state transitions, electrostatics of the high voltage acceleration and ion beam optics and the thermodynamics of the vacuum system made for a nice contrast to the confusing, and some times exhausting, process of troubleshooting and fixing everything that did not work with the experimental setup.

The majority of the time of this project was not spent doing experiments but rather on figuring out why you could not perform the experiments you wanted to. This, though energy consuming and a bit stressful, was in the end a rather positive experience that seemed quite indicative of experimental physics work in general. Everything does not turn out the way you want. It also transformed the experimental process into an opportunity of deeper learning that probably would not have occurred without encountering problems to the same extent. What this rather rocky road also thought me (basically hammered it in) was some valuable lessons about navigating accelerator experiments. Specifically that you should not jump to conclusions when thinking about possible causes of observed problems when dealing with complex systems.

The work in this thesis was performed primarily by myself and master student Jessica Warbinek, with occasional support from a Ph.d student named Annie Ringwall-Moberg, who primarily worked at another project at CERN. During the most intensive parts of the experimental setup troubleshooting, when we essentially disassembled the whole beam line, we received extensive help from Di Lu, Jakob Welander and Denisse Cruz. Felipe Ademir Aleman Hernandez helped when questions about the laser system arose. Jan-Åke Wiman also played a mayor role fixing and constructing new components and he was also kind enough to show me how to precision weld a new vacuum tight connection for the magnet. The intensive troubleshooting process (see documenting pictures in appendix A.3) is in part responsible for me wanting to have a rather detailed method chapter reflecting the amount of time spent examining the experimental setup.

To end this long winding preface I want to thank my supervisor Dag Hanstorp who not only answered all my questions but also introduced me to the simulation program SIMION and gave initial theoretical introductions to negative ions and lasers. He also tried to get me to keep my sentences shorter when writing my report (not always sucessfully). I also want to thank Johan Jellstam who let me borrow his computer and Di Lu for guiding me through his Chinese 3D-program and letting me construct some pictures from some of his 3D-models.

I hope that the reader finds this thesis interesting // Anton Krouthén 2020.06.04

2 Introduction

How can archaeologists know how long ago a mummy was a living person? How can geologists know the age of the earth? One answer is radiometric dating [1][2], a method that is used not only in archaeology and geology but also in such fields as environmental studies and physics. It can be used to date everything from the movement of glaciers and ground water to supernova explosions [3][4]. The basic principle of the method is to use the present-day abundance of a certain radioisotope in a sample and compare it to what would be the estimated starting point abundance of that radioisotope. In the case of ^{14}C, the probable choice of radioisotope for the mummy example [1], the starting point abundance would be the estimated equilibrium proportions of ^{14}C in the atmosphere (i.e at the time the person who became a mummy died) [5][6]. When a person dies no new ^{14}C will enter the body and, since ^{14}C is radioactive, the abundance of ^{14}C in the mummy will decrease over time. This type of radioactive behaviour analysis is the cornerstone of all radiometric dating and is what makes knowing the abundance of ^{14}C in a mummy-sample essential to the understanding of when that person died. [1]

One way to estimate the abundance of ^{14}C is to detect the amount of β-particles with the specific fingerprint-energy of the ^{14}C-beta decay that is emitted from the sample [7]. Unfortunately for ^{14}C, and for other long lived radioisotopes used for radiometric dating, the amount of decays you can detect from a sample during a reasonable measurement time is rather low (less than one millionth of the ^{14}C atoms in a sample will decay during the course of a day) [8]. This puts a constraint on how low abundances you can measure and also how small samples you can use. A way to overcome this is to use something called accelerator mass spectrometry (AMS).

AMS is a method that aims to break up the sample in ions of its fundamental atomic ingredients and basically count how much you have of each kind [9]. In the case of investigating ^{14}C abundances, AMS lets you directly detect all the ^{14}C atoms in a sample and not only the decays. The most limiting factor for the sensitivity of mass spectrometry measurements is the interference from isobaric atoms and molecules [8]. When you select ions with a mass spectrometer you get what the name implies, ions with the same mass. If you want to measure the abundance of a certain isotope of a particular element you may still have contaminations from other elements that have either isotopes or molecular configurations with the same mass (isobars). The development of suppression methods for isobar-contaminants has been a central focus of AMS research the last 40 years and has made AMS into the astonishingly powerful analytic tool it is today. Satisfactory abundance measurement results have been achieved even when the abundance of the isotope of interest is as low as 10^{-16} [8][10]. This result has been described as looking for a few specific needles in an enormous stack of needles (one sought needle per ten thousand trillion needles).

This project is related to on one of the suppression methods called selective laser photodetachment. The method utilizes differences in electron affinity (EA), a measurement of how tightly the extra electron of a negative ion is bound [11], to selectively neutralise contaminants and isolate ions of interest [12]. The fact that all AMS systems allready start with the creation of negative ions [13] is the key to the possibility of this relatively newly adopted method to be used more extensively in the future. The hope is that the method can be used in cases where other suppression methods still aren't able to achieve satisfactory isolation [14].

Unfortunately there is one inconvenience with selective laser photodetachment suppression. You can only suppress interferences from elements with lower EA than the element of interest. When this is a problem you try to overcome it by looking for a molecular system where the order of EAs are reversed and you are able to suppress only the contaminant [12]. Researchers at Vienna Enviromental Research Accelerator (VERA) want to find a molecular system for which a specific laser wavelength can neutralize as much ^{107}Ag (silver) as possible while keeping basically all of the usually much less abundant radioisotope ^{107}Pd (palladium) negatively charged. Molecular systems of Ag and Pd are investigated because of the fact mentioned above: atomic silver has a higher EA than atomic palladium [15][16] which makes straightforward selective laser photodetchment of atomic silver impossible. The first stepping stone in this search is to investigate the easily produced oxide versions.

The necessary experiments investigating the behaviour of anionic PdO (EA=1.672 eV [17]) and AgO (EA=1.654 eV [18]) would be hard to carry out at the VERA facility without contaminating their high precision AMS system with unwanted alloys. Experiments was therefore carried out at Gothenburg University Negative Ion Laser LAboratory (GUNILLA).

This project aims to use laser photodetachment threshold spectroscopy (LPTS) to measure the relative photodetachment cross section of AgO and PdO with respect to Ag for different laser wavelengths. The photodetachment cross section behaviour for atomic oxygen will also be experimentally investigated as a proof of principle. The absolute photodetachment crossection of atomic silver was measured in a parallel project at UC Louvain in Belgium and their results will later be used to extract absolute photodetachment cross section values for PdO and AgO, if they are suitable candidates for ^{107}Ag suppression. The experiments carried out at GUNILLA aims to answer the central question:

Is PdO and AgO suitable molecular systems for selective laser photodetachment suppression of ^{107}*Ag when investigating the abundance of* ^{107}*Pd with AMS? And if so what laser wavelength would be optimal to use?*

3 Basic theory and background

3.1 Negative ions

Negative ions is a very interesting, some say exotic, research subject. From first principles of electrostatics it may seem hard to understand how they can exist in the first place. Why would a neutral atom or molecule attract an extra electron to create a negative ion?

Even if we use quantum mechanical calculations within the independent particle approximation of atomic physics we will get little help predicting the behaviour of negative ions. Though it might give us the idea that what is essential to the formation of negative ions is exactly what is missing from the independent particle model: the part of the binding energy that comes from the correlated motions of multiple electrons [11].

How is the wave function and probability distribution of the position of one bound electron affected by the specific wave function/probability distribution of the position of another electron? This is a question that the investigation of negative ions can help shed light on. Apart from being important for the general understanding of the structure and dynamics of many electron systems [19], the focus on electron correlations can help us introduce a semi-classical description of why negative ions can exist in the first place: *If an electron is brought close to an atom it should repel the electrons bound to that atom. This will affect the probability distributions of those bound electrons and induce an electric dipole potential which can attract and trap the free electron that induced it.* The binding energy of this trapped electron, how much the energy of an atom is lowered by the binding of an extra electron, is what is called the electron affinity (EA). You can say that it is a measurement of how much the atom likes and has a tendency to attract the electron. In more scientifically rigorous terms, the EA is dependent on the polarizability of the atom (or molecule) and is defined as the difference in the total energy between the ground state of the neutral atom or molecule A and the ground state of the corresponding negative ion A^- [11].

$$EA(A) = E_{tot}(A) - E_{tot}(A^-) \tag{1}$$

3.1.1 Photodetachment

Photodetachment is when a photon with high enough energy (energy over the photodetachment threshold) is absorbed by a negative ion and this negative ion splits up in a neutral atom (or molecule) and a free electron.

$$A^- + \gamma \rightarrow A + e^- \tag{2}$$

It is however not the case that as long as the energy of photons in a laser beam is higher than the EA of the ions in a overlapping ion beam all the ions will suddenly become neutralized. The photodetachment probability starts at zero at the energy threshold value, which in itself is a bit strange compared to the finite value characteristic of photoionization cross sections. It then rises with higher photon energy but sometimes in different ways for different elements. It also tops at photon energies of a few eV to tens of eV above the photodetachment threshold and asymptotically approaches zero at higher energies. [19]

To understand why this is the case we can start by looking at the photoabsorption probability described by Fermi's golden rule[11]:

$$P_d = \frac{2\pi}{\hbar} | \langle \psi_f | D | \psi_i \rangle |^2 \rho_f \tag{3}$$

where the probability P_d of a transition from an initial state $|\psi_i\rangle$ of the later ejected electron to the final continuum state $\langle \psi_f|$ is dependent on the overlap of the states, the electric dipole operator D and the density of final states ρ_f. The electric dipole operator D can be seen as the transformation matrix corresponding to the photoabsorbtion process and the value of ρ_f, the desity of final states, depends on the energy ϵ of the ejected electron.

$$\rho_f \propto \sqrt{\epsilon} \tag{4}$$

The photodetachment probability decline for higher photon energies is due to the declining overlap between the initial bound state wave function and the rapidly oscillating wave function representing the emitted electron. [19] What about the weird differences in the photodetachment probability for different elements when you increase the photon energy near the photodetachment threshold energy? Directly after photoabsorbtion you can again look at the system from the semiclassical perspective. As soon as the electron is in its final state with just high enough energy to overcome the induced electric dipole pontential $\propto r^{-4}$, it will be allowed to find itself at larger distances r from the nucleus. At this stage when the electron is no longer inducing a dipole potential but the ejection energy is still small (photon energies near EA threshold) the centrifugal barrier becomes a dominating factor dictating the behaviour of the photodetachment probability and thus the photodetachment cross section σ. Together with equations (3) and (4) this leads to something referred to as the Wigner threshold law [11]

$$\sigma \propto k^{2l+1}, \tag{5}$$

where k is the linear momentum and l the angular momentum of the ejected electron. This is obviously not only pointing to the importance of the angular momentum part of the ejected electron but also of the initial state of this electron.

The answer to why is the concept of conservation of angular momentum. Since the incoming photon has an angular momentum of one ($l = 1$) the change between the initial and final state of the electron must be ± 1. For an initial state of $l = 0$ the final state will have $l = 1$ and for initial states with $l > 0$, $\Delta l = -1$ will dominate near the EA threshold. The photodetachment cross section behaviour near the EA threshold is generally called a *s*-wave for ejected electrons with angular momentum zero and *p*-wave for electrons with angular momentum one[11] (figure 1).

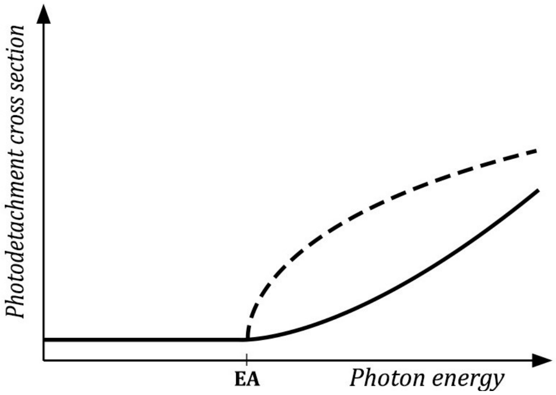

Figure 1: *Shape of photodetachment cross section around the EA treshold for an ejected s-wave electron (dashed line) and a p-wave electron (solid line).*

For many elements the the observed cross section shape will deviate somewhat from the clear *s*- or *p*- wave visualized in figure 1 due to for example fine structure splitting [20][21] (visualised in figure 2).

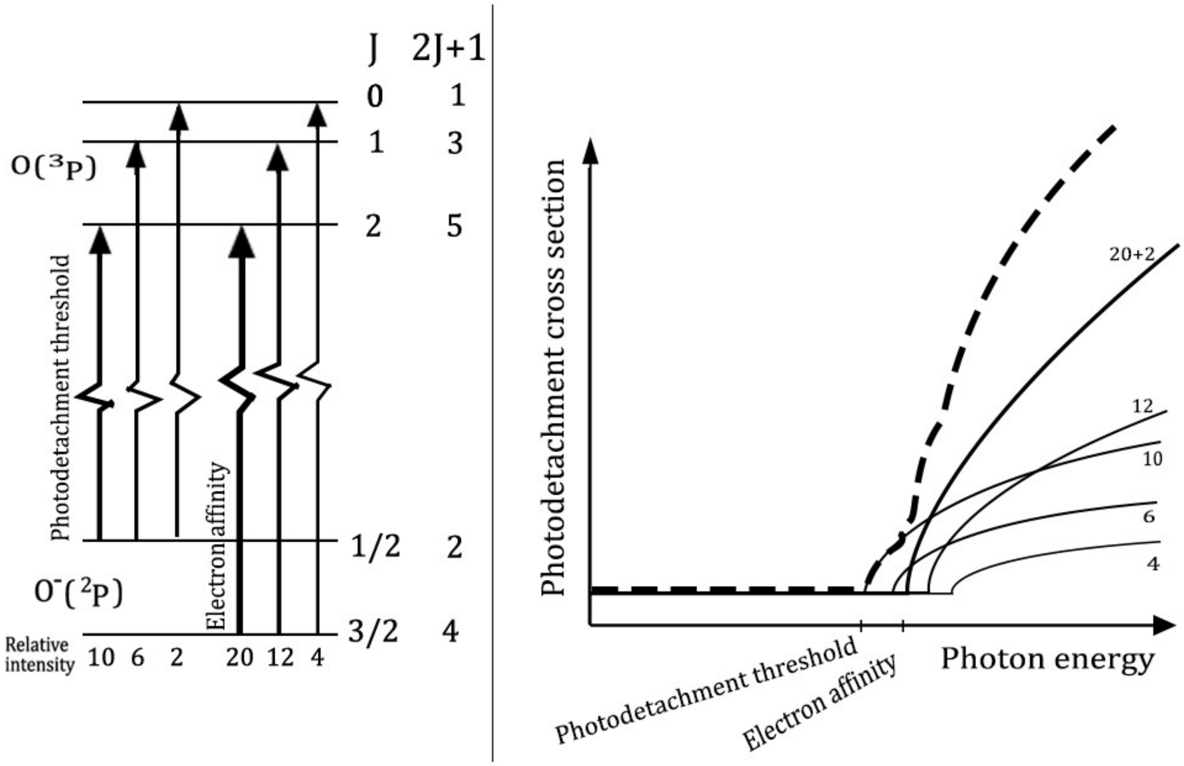

Figure 2: *Photon absorption transitions from anionic oxygen to neutral oxygen (left) and corresponding* O^- *photodetachment cross section shape (right). Probability weights (relative intensity) of the different transitions are marked with numbers beneath transitions and beside solid cross section lines corresponding to the specific transitions. The dashed line visualises the shape of what would be the observed total photodetachment cross section behaviour.*

3.1.2 Photodetachment of molecular negative ions

A big difference between photodetachment of atomic and molecular negative ions comes from the obvious difference between the structural similarity of atoms and the variability of molecular structures (both in size and shape). In molecules you also have the possibility of rotational and vibrational exited states in both neutrals and anions. If a photoabsorbtion induced transition from anion to neutral ground state involves a molecular structure rearrangement it could be that the transition to some rotational-/vibrational exited state of the neutral is more probable than a transition to the ground state [11]. If the molecular ions are not sufficiently cold it is probable that they are in some exited vibrational state to start with when interacting with the laser [14]. This makes the photodetachment cross section shape around the EA threshold less distinct than in the atomic cases.

3.2 Radioisotopes and AMS

Only five radioisotopes were pursued at the beginning of AMS research but over time many more became available. In 2013 a list of 55 radioisotopes used in AMS was published [8]. The motivation behind investigating the possibility of AMS studies of ^{107}Pd, the radioisotope of interest in this project, is the general developmental goal of enlarging the toolbelt of available radioisotopes at VERA in the specific half life interval around the half life of ^{107}Pd (6,5x10^6 y). AMS measurements of different radioisotopes is not only used for direct dating of certain events but is also used for the improvement of half life estimates of radioisotopes where the uncertainty of the half life is unsatisfactory.

AMS research can also be a critical component of other research projects in physics such as those investigating nucleosynthesis processes. A current project at VERA is looking at questions that might give information on what process, supernova or neutron star merger, is the most probable cause of creating a majority of the heavy elements in the universe. This is achieved by looking at the contents of deep sea drilling samples containing ^{60}Fe that is concluded to come from when the earth was showered with materials from a supernova explosion. Analysing the contents of those samples and finding other elements with the same age and probable origin (radiodating) can give information about nucleosynthesis in supernova explosions and guide researchers in the investigation into the origin of elements.

One possible application of AMS studies of ^{107}Pd is to precisely measure the ^{107}Pd abundance in magmatic iron meteorites. This is of potential interest when investigating early planetary formation in the solarsystem (protoplanets) [22]. The isotope content of the meteorites can give you information about the cooling processes of the metallic core of protoplanets and also information about possible meteoroid collisions with these early celestial bodies [22]. This is presently done by Pd-Ag chronometry where you estimate earlier abundances of ^{107}Pd by measuring the excess ^{107}Ag in meteorites compared to terrestrial averages. The excess is concluded to come from the decay of now extinct ^{107}Pd that was present in the early solar system. [23] The possibility of measuring live ^{107}Pd (even at very low abundances) could be valuable as an additional input when correcting the calculations of the protoplanet formation for cosmic radiation effects on the meteors on their way to earth [24].

3.2.1 Layout of a typical AMS system

Even though significant progress has been made since the first AMS system was built some fundamental principles and components still remain as the basis for modern systems [13]. AMS systems can in general be divided into five consecutive processes (schematics shown in figure 3).

1. **Ion Source-** Practically all contemporary AMS systems start with a cesium sputter ion source [25], the same type of ion source used for this project at GUNILLA (more on this in the method chapter). The Cs sputter source is used for its high efficiency regarding negative ion formation, relatively good beam current stability and short switching times for sample cathodes [13].

2. **Low energy mass analysis-** The particles in the beam formed from the sample gets their first sorting by mass in a simple low energy magnetic dipole spectrometer. This works very well for separating lighter elements but for i.e actinides more sophisticated methods are preferable. [13]

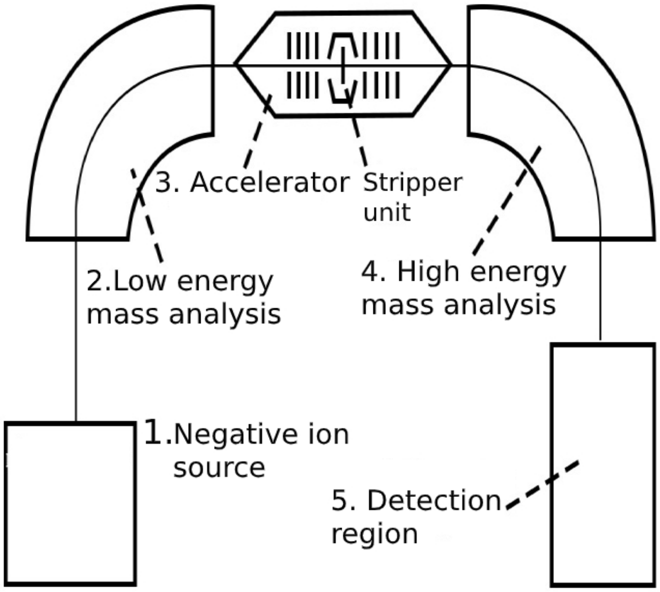

Figure 3: *Schematic sketch of a typical AMS system*

3. **Accelerator-** This is the central part of an AMS-system that separates it from regular mass spectrometry. After the negative ions are accelerated to energies ranging from 0.2 to 25 MeV (depending on the system) they are injected to something called the charge exchange system or the stripper unit [13]. This is either a windowless gas filled cell or a thin foil. When the ions penetrate the medium, collisions will occur and electrons will be stripped off the incoming negative ions. When they are stripped from multiple electrons (not only the one making it net negatively charged) and charge states higher than 2+ are populated, molecules in the beam will dissociate by the strong repulsive coulomb force present by the absence of electrons. The now positively charged atomic ions are guided to the next filtering step of the AMS process.

4. **High energy mass analysis-** After the stripping process a second mass analysis of the beam takes place to single out atomic ions with the same mass. The higher beam energy gives the possibility for greater accuracy and both momentum over charge (p/q) analysis and energy over charge (E/q) are used to unambiguously identify the mass of the ions [13]. It is also at this point in the setup that you can get information on other elements in the sample that need less accurate measurement techniques. This is usually needed to analyse ratios between them and the rare radioisotope of interest. The aim of AMS is as pointed out earlier to measure abundances and the ratios between elements and isotopes are therby of interest.

5. **Single ion detection and identification-** For the final stage of an AMS-setup silicon solid state detectors as well as gas ionization chambers are used to detect and identify the particles under investigation [13].

3.3 Isobar suppression

The interference of isobaric contaminants is as mentioned in the introduction the biggest problem affecting the signal to background ratio of AMS measurements. There exists a stable isotope for almost every element from ^{2}H up to ^{208}Pb, excluding technetium (Z=43) and promethium (Z=61). Thees stable isotopes will usually be far more abundant than the rare radioisotopes you are interested in. The main methods of suppressing unwanted isobars are listed in the upcoming subsections and connected to the layout description of the typical AMS setup.

3.3.1 Chemical preparation of sample

Typical original samples (water, rocks etc.) does not have a high enough concentration of radioisotopes to directly use them in AMS [26]. If you would try to use these original samples (in the size range of 100 g- 10 kg) you would run into similar problems as in the decay detection method mentioned in the introduction. To overcome this problem in AMS you use samples that have been chemically treated to be smaller and more concentrated.Typical samples used in AMS are after chemical treatment in the 1 mg range. This chemical separation turns out to also be a good suppression method for some unwanted isobars. Not only can you suppress interfering elements [27] but you can also at times separate ”versions” of the same isotope (versions = isotopes that are created or accumulated in different ways). One example is the analysis of cosmogenic ^{10}Be in quartz where you chemically separate interfering atmospherically-produced ^{10}Be [28][26].

3.3.2 Ion formation

This first part of an AMS setup, the negative ion formation from the sample, turns out to be a good isobar suppression method for certain radioisotopes. Primarily the suppression of ^{14}N when investigating abundances of ^{14}C. ^{14}N contamination is completely eliminated by the fact that nitrogen does not form negative ions [11].

3.3.3 Molecule destruction

Contaminating molecular isobars (i.e. CH_2 to ^{14}C) are suppressed by the destruction of molecules in the stripper unit after the accelerator. Since molecules decompose into their atomic ingredients in this part of the setup molecular isobars simply no longer exist after this point in the beam line.

3.3.4 Specific energy loss separation

This category of separation methods is the main form of isobar suppression responsible for the overall usefulness of AMS measurments [13]. The methods uses the difference in stopping power needed for different elements (dependent on the proton number of the nucleus). It is mainly utilized in the detector region of the AMS setup where different types of detection methods can use the principle of specific energy loss to identify elements and, by the fact that the particles are already sorted by mass, specific radioisotopes. Detection methods commonly used are ionization chambers and gas filled magnets. The main problem with this category of isobar suppression is the fact that the measurable difference in energy loss between elements decrease with higher proton numbers (visualized in figure 4).

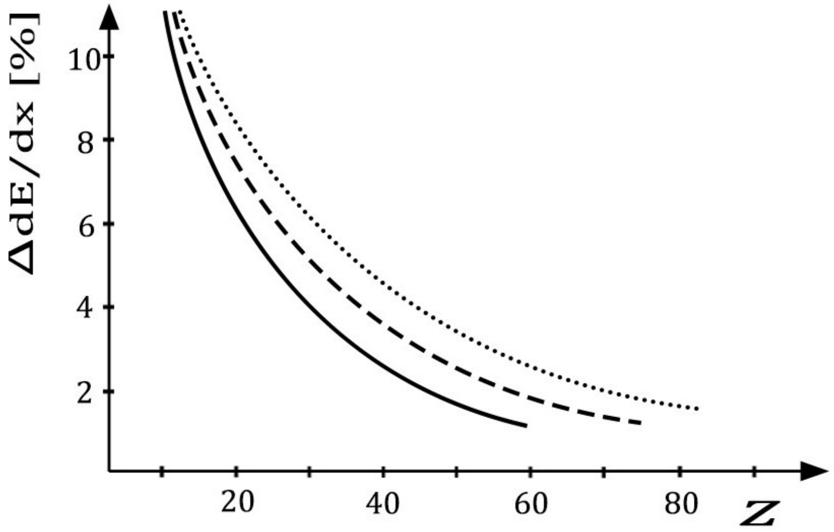

Figure 4: *Percentile difference in energy loss for neighbouring elements (Z). Different lines represent different beam energies (solid= 1 Mev/amu, dashed= 2 Mev/amu, dotted= 4 Mev/amu).*

This decrease is, as can be seen in figure 4, combated by increasing the acceleration energy of the system. Small elements like ^{10}Be, ^{36}Cl and ^{41}Ca can be measured with a terminal accelerator voltage of 5 MV resulting in energies around 1 MeV/amu. For elements in the medium mass range, like ^{60}Fe and ^{63}Ni, you often use accelerators with terminal voltages up to 14 MV (resulting in energies around 2-3 MeV/amu) [13]. For even larger elements the ionization chambers and gas filled magnets can no longer achieve satisfactory distinction between elements. One detection method with somewhat larger range is ΔTOF measurements. It uses the measurable difference in energy loss between elements when isoenergetic ions pass through something called energy degrader foils. After passing the foils different elements will have different velocities which makes it possible to distinguish them in a time-of-flight measurment [29] (using the silicon solid state detectors mentioned in the AMS description chapter).

3.3.5 Selective laser Photodetachment

Although the idea of selective laser photodetachment as a suppression technique almost is as old as AMS itself, it is only quite recently that it became a viable alternative to use when other suppression methods gives unsatisfactory results. Before Radio Frequency Quadrupole (RFQ) cooling for anionic beams was a realistic option the interaction times between laser light and anions would be far too short to achieve satisfactory suppression from selective laser photodetachment. The introduction of RFQ cooling made the interaction times between ions and laser light sufficiently long to facilitate satisfactory isobar suppression with commercially available lasers. The ILIAMS project, the RFQ cooler setup for selective laser photodetachment at VERA (layout shown in figure 5), has achieved suppression factors of over ten orders of magnitude. [12]

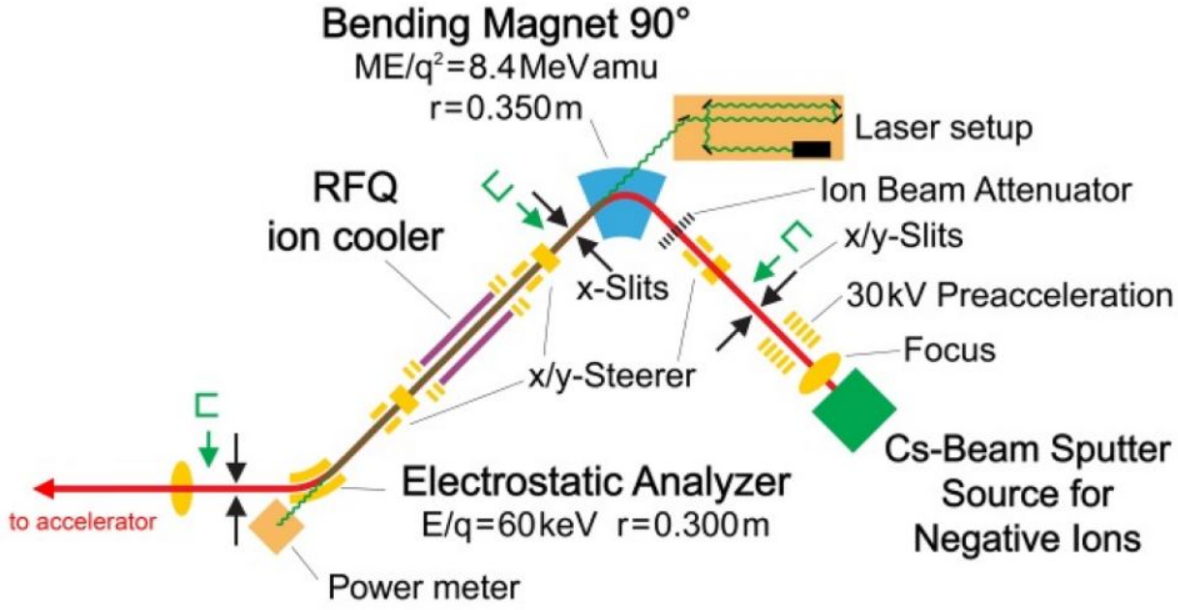

Figure 5: *Schematic sketch of ILIAMS at VERA, illustration by Martin Martschini [12]*

To achieve satisfactory suppression the best case scenario can be described as a case where the photodetachment cross section of the two elements we want to separate both show the behaviour of *s*- waves with the contaminant having the lowest EA. With this being the case you can choose a laser wavelength (preferably cheap and easy to produce) where you can maximise the neutralisation probability of the interfering ions while still keeping all the ions of interest negatively charged (visualised in figure 6). This behaviour is what is investigated with LPTS.

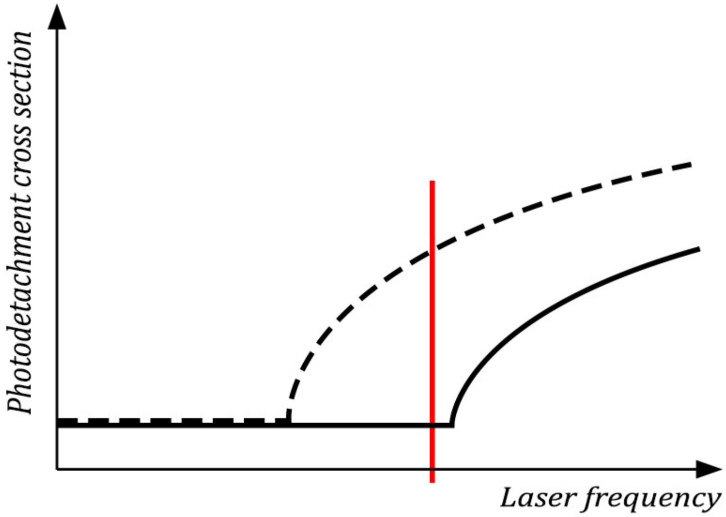

Figure 6: *Optimal photodetachment cross section behaviour for selective laser photodetachment (dashed line = contaminant, solid line = ion of interest). The vertical line represents a possible choice of fixed laser frequency for optimal suppression.*

4 Method

To perform Laser Photodetachment Threshold Spectroscopy (LPTS) on O^-, Ag^-, PdO^- and AgO^- the negative ion accelerator (figure 7) and connected laser system of GUNILLA was used. The different relevant sections and parts of the system are listed and explained in upcoming subsections.

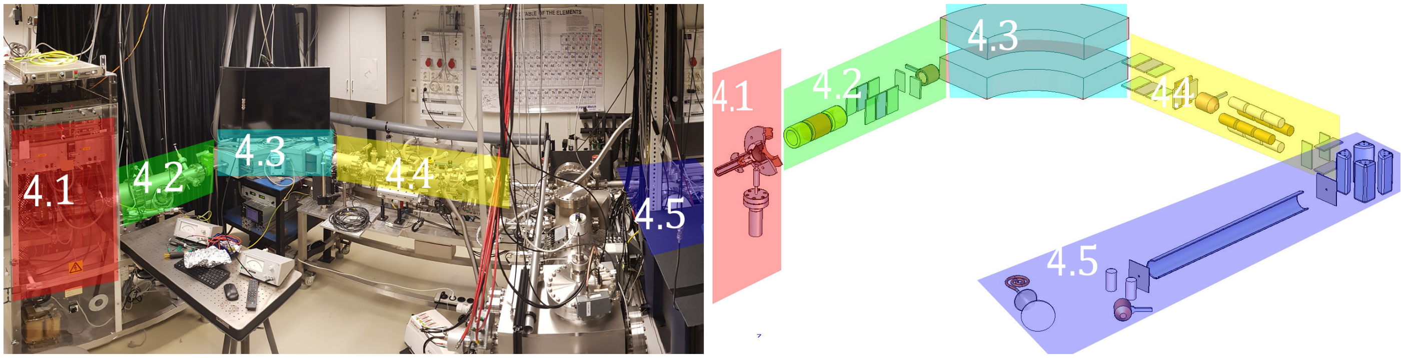

Figure 7: *Section layout of GUNILLA. Numbers in colored regions represents sections of the setup described in upcoming sections of the text.*

4.1 Negative ion source

The basic principle of the cesium sputter source is that a sample cathode is bombarded with positive cesium ions to sputter out negative ions to accelerate into the beam line. The source (Fig. 8) consists of several parts described below.

4.1.1 Sample cathode

The sample cathode is a solid aluminum cylinder into which a small hole is drilled. This hole is packed with a PdO/AgO mixture powder (50/50 ratio). A power supply is connected to the electrically conductive cathode to put it at a static voltage of -6 kV compared to ground and water cooling is connected to avoid heat buildup during sputtering.

4.1.2 Cesium reservoir

Below the cathode is a small cesium reservoir wrapped with heating wire to put it at a temperature of approximately 80°C.

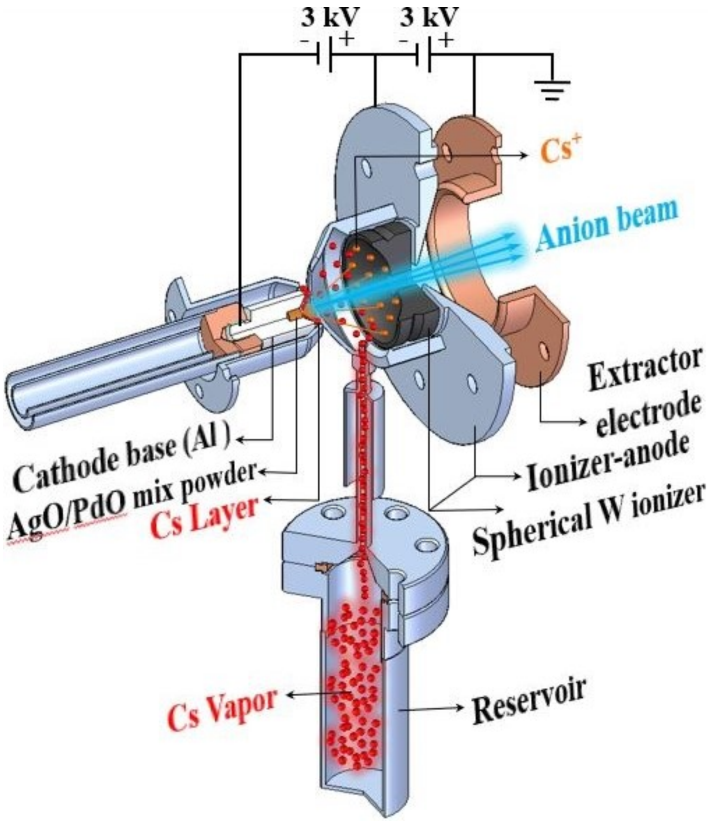

Figure 8: *Source schematics*

The fact that the source is under high vacuum makes the temperature of 80°C high enough to turn a sufficient amount of cesium into vapour even though cesium evaporates at 671°C at sea level (1 atm pressure) [30]. Sputtering intensity can be regulated by changing the cesium reservoir temperature but higher temperatures makes the experiment running time shorter. Both the life time of the sample and the cesium reservoir depends on the sputtering intensity. A feed tube, also wrapped with heating wire, connects the cesium resevoir to a chamber where the cesium particles are ionized. This tube is generally set at a temperature of 220°C but both the feed tube and the reservoir temperatures can be varied as a tool to combat unsatisfactory beam behaviour (fluctuating beam stability).

4.1.3 Thermal ionization of cesium

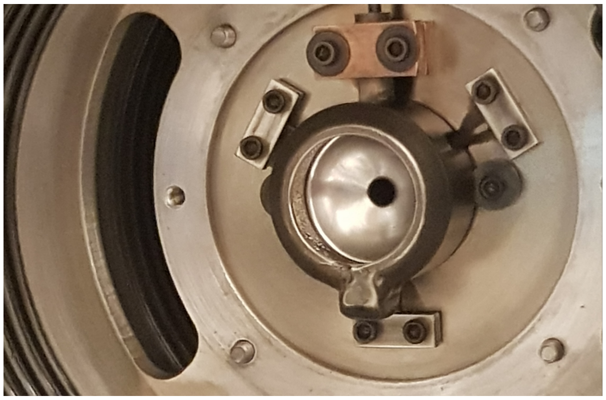

Figure 9: *Picture of ionizer*

The gas from the cesium reservoir enters a chamber where it is thermally ionized by a spherical ionizer (a miniature ”satellite dish”, see figure 8 and 9) made of the material tungsten (W). The ionizer is set at a temperature of 1200°C and put at a voltage of -3kV compared to ground.

4.1.4 Sputtering and acceleration

The geometry of the ionizer and the difference in potential will accelerate and focus the Cs^+ ions to mainly hit the Ago/PdO-powder in the cathode and sputter out atomic and molecular fragments of this material. It will also form a small Cs layer on the cathode surface which will lower the workfunction and increase the probability of electron donations to the sputtered material [11]. The newly formed negative ions will be accelerated through a hole in the ionizer by the same field that accelerated the positive ions in the other direction. The negative ions are further accelerated with another 3 kV by the extractor electrode (figure 8).

4.2 Beamline ion optics section 1

When the ions enter the beamline they will diverge (figure 8, 10, 13). The ion beam is therefore focused by several electrostatic lenses throughout the beamline (figure 13). The first section of the beamline, between the ion source and the bending magnet, consists of an einzel lens followed by a x-lens and a x-slit.

- The **einzel lens** is three consecutive cylindrical electrodes where the first two are grounded and the middle one is put on high voltage. This focuses the beam with cylindrical symmetry as shown in figure 10 and 11 (beam size exaggerated for visual effect).

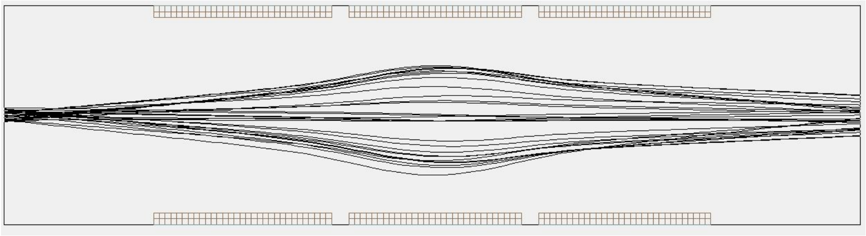

Figure 10: *Einzel lens simulation SIMION - cross section*

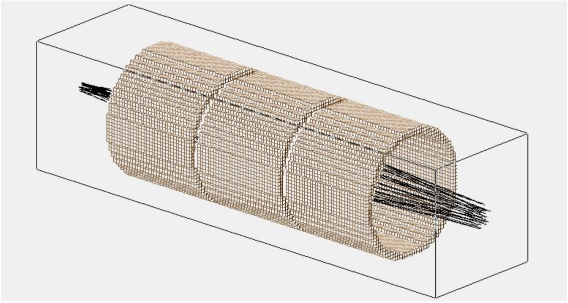

Figure 11: *Einzel lens simulation SIMION*

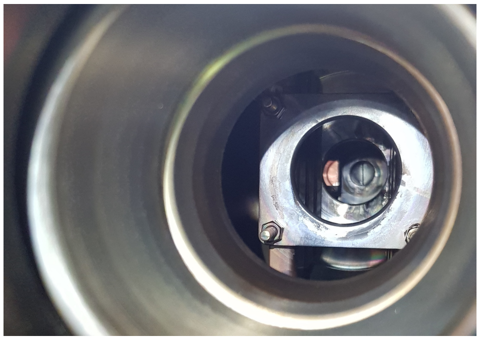

Figure 12: *Picture looking into the beamline from the position of the ion source. Starting with cylindrical electrodes of the einzel lens, flat electrodes of the x-lens and the x-slit.*

- The **x-lens** works in the same way as the einzel lens with the difference that it does not have cylindrical symmetry. Instead it is three consecutive pairs of flat electrodes focusing the beam in the horizontal x-direction (similar to the einzel lens cross section visualized in figure 10).

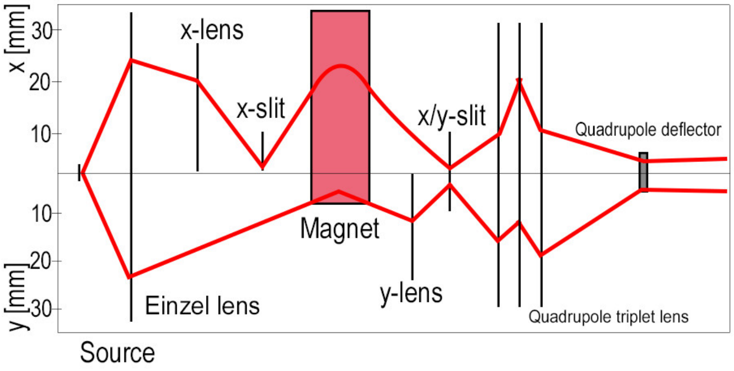

Figure 13: *Approximate visualisation of beam width in x- and y-direction at different beamline components. The specific behaviour is defined by what settings you use for the electrostatic lenses.*

After the x-slit a Faraday-cup is placed as the first analysing point. A Faraday-cup is basically an electrically connected conductive plate or cup you can insert on demand to block the beam and measure a current from when it is hit by charged particles.

4.3 Bending magnet

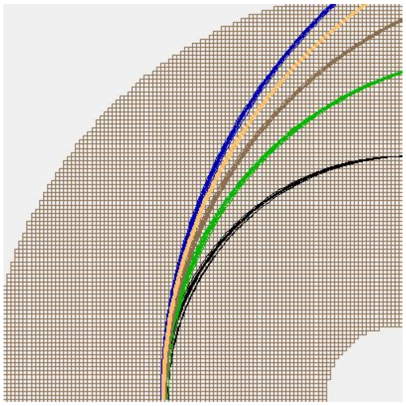

Figure 14: *SIMION simulation of particle trajectories due to bending magnet. Different colors are trajectories of particles with different mass*

Trajectories of charged particles can be bent by the Lorenz force in the pressence of a magnetic field:

$$ma = qv \times B \tag{6}$$

Particles with different mass entering the bending magnet will end up on different trajectories due to their difference in mass (see figure 14). By varying the magnetic field strength you can choose which mass you want to isolate. A larger current supplying the electromagnet creates a stronger magnetic field which means that the trajectories gets more bent and heavier particles are exiting the magnet.

4.4 Beamline ion optics section 2

After the bending magnet the beamline consists of a y-lens followed by a x- and y-slit, a second Faraday-cup, a quadrupole triplet lens and a x/y-deflector (schematics in figure 15).

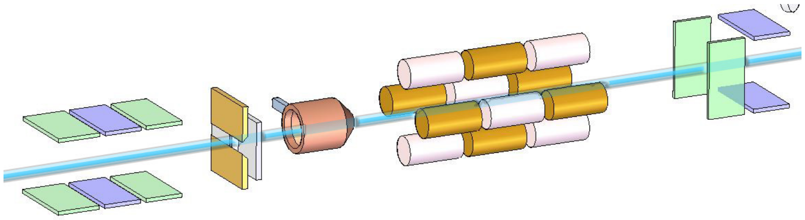

Figure 15: *Schematics of beam line optics section 2. Beam direction from left to right.*

- The **y-lens** works exactly as the x-lens but rotated 90 degrees to focus the beam in the y-direction.

- A **quadrupole triplet lens** is a bit more complicated. It consists of three consecutive sections of four rounded, rod- like electrodes lying parallel to the beam direction (see figures 15 and 16). Electrodes with the same color in figure 15 will have the same charge sign (positive/negative) which will result in alternating lens effects in the x- and y-direction. When the ions pass from the first to second section the beam will focus in the y-direction and defocus in the x-direction (figure 13). When they pass from the second to third section it will do the opposite. The shape of the electric fields between the sections and the resulting particle trajectories (divergence/convergence and acceleration and deceleration) will result in a net focusing effect in both x- and y-direction. This lens is used to finally tune/combat the beam behaviour difference in x- and y-direction created by the magnet (focusing in the x-direction, see figure 13 and 14).

- A **x/y- deflector** (right end of figure 15) is consisting of electrodes connected in such a way that you are able to push the beam up/down and to the sides by changing the voltages on the deflector electrodes.

Figure 16: *Picture looking into the beam line through the exit of the quadrupole triplet lens*

4.5 Quadrupole deflector, laser beam entrance, interaction region and detector

The fifth section of the system (as specified/divided in picture 7) starts with a quadrupole deflector bending the beam 90 degrees to overlap the incoming laser beam (see figure 17 and 18). This is done by having the four vertical rod-like electrodes configured in a way so that diagonally opposite electrodes has the same charge and the electrode to the side has the opposite charge (positive/negative). The possibility of interactions between photons and ions starts where the ion beam is bent by the quadrupole deflector and it overlaps the laser beam.

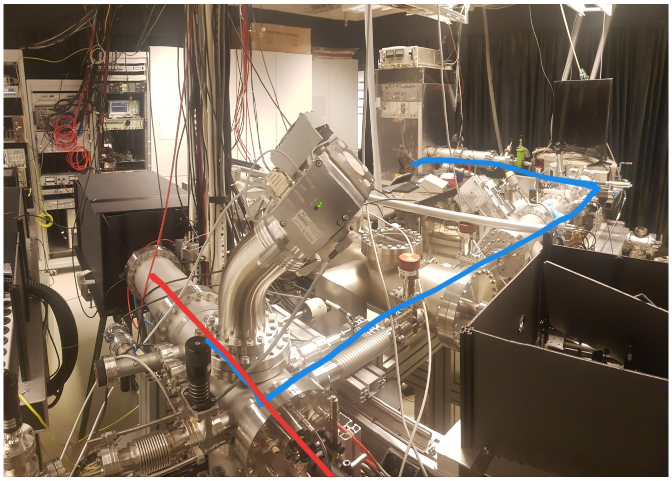

Figure 17: *Picture of the beam line from the entrance of the laser beam.*

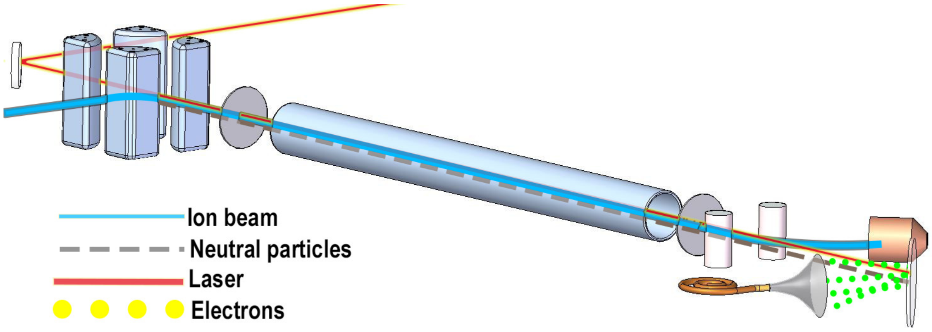

Figure 18: *Schematics of the fifth section of GUNILLA*

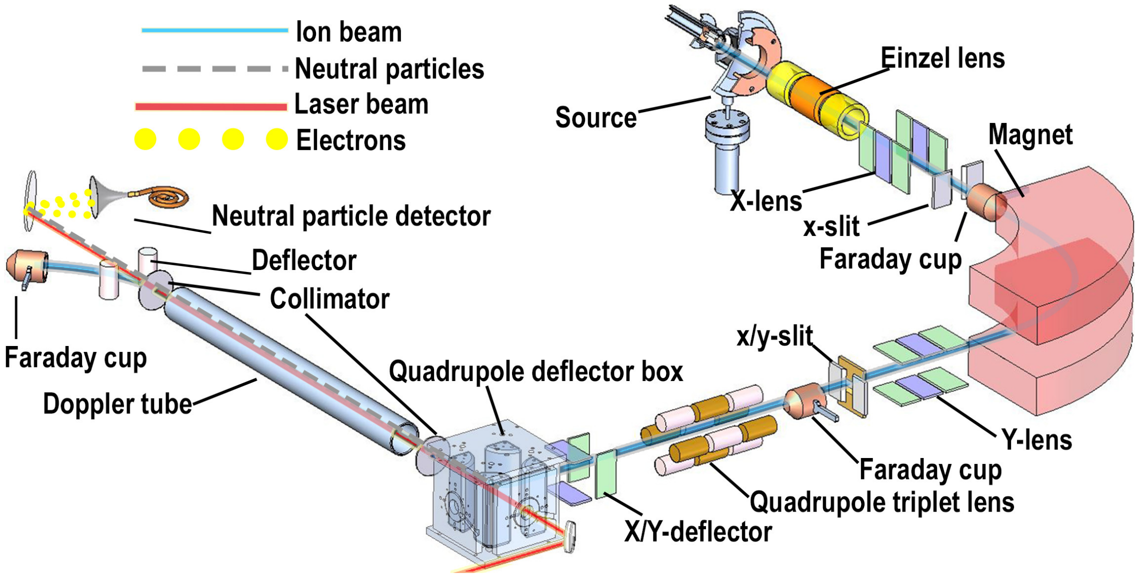

Figure 19: *Component overview of GUNILLA*

The interaction region consists of an entrance collimator, a doppler tube, a second collimator and at the end a deflector to deflect particles that still have charge after the interaction region into a final Faraday-cup. The ions that have lost an electron in the interaction region and have become neutrally charged will not be deflected and continue straight into a neutral particle detector (schematics in figure 18 and 19 and components not yet described are listed below).

- A **collimator** is an electrically conductive metal plate with a hole in the middle letting the ion beam through. At an early stage of optimizing the ion optics when the charge on the quadrupole deflector electrodes is initially increased, to bend the incoming ion beam, you can get information on how bent the beam is by monitoring the current from the first collimator connected to an ampere meter. This is helpful if you can not observe a current from the last Faraday-cup (the collimator can act as a larger target to help you find the beam). The collimator plates can also be used to align the beam line during assembly.

- The **doppler tube** is enclosing the ion beam in the interaction region and can be put on a potential to accellerate or decellerate the ions entering the tube to doppler tune the interaction frequency of the laser light. Co-linear laser interactions will see doppler-shifts and this has to be corrected to yield exact values of the EA.

- The **neutral particle detector** counts single particles by detecting bursts of electrons being ejected from a material when it is hit by a neutral particle. The detector is triggered by the laser pulse with a delay corresponding to the travel time of the particles.

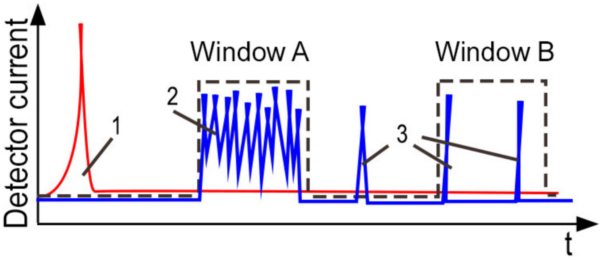

Figure 20: *Detection of laser pulse (1), neutral particles from photodetachment (2) and background (3).*

The delay time is dependent on what element is being investigated (since the mass will determine the speed of the ions after the initial acceleration). Neutral particle counts are accumulated during a time window (A) starting when the first particles (that at the time of the laser pulse are closest to the detector) arrive to the arrival of the particles that at the time of the laser pulse are the furthest away from the detector, but still in the interaction region (basically inside the quadrupole deflector). Neutral particle counts are also accumulated under a second time window (B), corresponding to when there is no laser pulse interacting with the ion beam (background measurement). Since there is no perfect vacuum, and you also have random internal particle collisions neutralizing ions inside the ion beam, you will always have some interfering stray particles hitting the detector that does not come from the photodetachment process.

For the oxygen measurment the delay time between the laser pulse and the photodetachment detection window (window A) was set to 0,9 μs with a window width of 2,5 μs. The delay time for the background detection window (window B) was set to 30 μs with the same window width of 2,5 μs. For the other measurments the delay time was set to 2,3 μs for window A and 30 μs for window B with window widths of 4,8 μs. An oscilloscope connected to the detector is checked so that all neutral particle detections from the laser pulse photodetachments arrive ”inside” detection window A.

4.6 Vacuum system

Throughout the beam line there are several vacuum pumps keeping the system at pressure levels from 10^{-6}mbar at the source to 10^{-9}mbar in the interaction/ detector region. There are two initial vacuum pumps pumping down the system from air pressure after assembly/maintenance, one multi stage root pump and one rotary vane pump. There are also at least one turbomolecular pump per section of the beam line used to reach and maintain high vacuum.

- A **multi stage root pump** is a dry pump meaning there is no oil or fluid used to pump down the system. The pump consists of stages of rotors compressing and transporting the gas/ air sucked in from the system you want to pump down.

- A **rotary vane pump** is similar to the multi stage root pump with the difference that its main suction comes from one big rotating cylinder with movable plates sticking out pushing the gas/air from the inlet further into the pump.

- A **turbomolecular pump** is a pump that needs sufficient vacuum (0,1 mbar) already at startup to not be damaged. It consists of a number of rapidly spinning fans/rotors with the blades configured so that the atoms and molecules hitting the blades will be directed out of the system you want to pump down (also called momentum transfer pump).

4.7 Laser system

The laser system used is a tunable titanium sapphire (Ti:Sa) laser pumped with a 10 ns pulsed frequency doubled Nd:Yag (neodymium-doped yttrium aluminum garnet) laser. The output is a narrow linewidth beam that in the main experiment is scanned in the λ-interval 900 nm - 700 nm. The interval selection is based on earlier experimental EA estimations of AgO^- and PdO^-. The EA estimates are 1.654 eV (749.6 nm) [18] for AgO^- and 1.672 eV (741.53 nm) [17] for PdO^-. The layout of the Ti:Sa laser is visualized in figure 21 and described below.

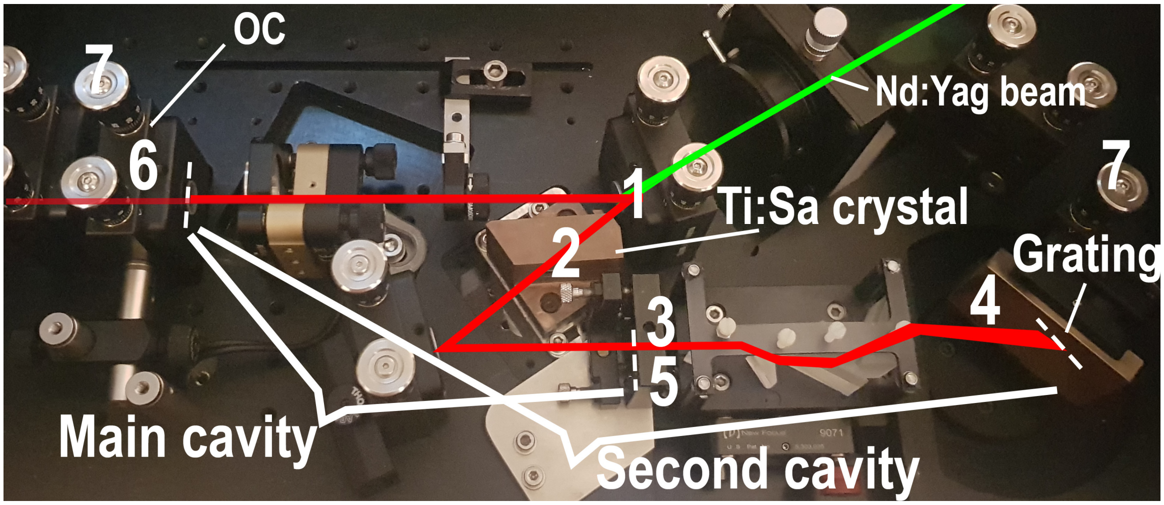

Figure 21: *Ti:Sa laser: Numbers 1-7 correspond to description list numbers below.*

1. Incoming Nd:Yag laser light passes through a sapphire crystal (Al_2O_3) doped with Ti^{3+} ions and photon absorption in the material makes exited states become populated (called pumping).

2. Stimulated emissions from a wide range of transitions (broad band) are induced by standing waves allowed in the main laser cavity (initially produced from spontaneous emission after the pumping).

3. A semi transparent (40%) mirror lets the light from the main cavity pass into a region of prisms expanding the beam profile before it hits a tunable grating.

4. The angle of the grating chooses around what wavelength standing waves will be allowed in the second overlapping cavity. What standing waves are allowed in this longer cavity depends on the variable length of that cavity and will have narrower bandwidth than the ”initial” broad band signal leaving the main cavity. You can also look at it like if some frequencies are not allowed to be reflected from the grating and travel back into the main cavity.

5. The new narrow bandwidth standing wave ”seeds” enters the main cavity and stimulate emissions from the crystal in a narrower frequency interval which ”over time” (for photons so basically instantly) builds up the power of the light (standing waves) in this frequency interval in both cavities and makes it dominate.

6. Laser light is emitted through the output coupler (OC) at 20% transmission, focused further with a telescope and guided with mirrors into the interaction region of the beam line. The specific transmission percentage is chosen to maximize output power. The transmission percentage becomes a trade-off between having high transmission to increase output power and having enough reflection to keep the laser power in the main cavity sufficiently high to stimulate enough new transitions in the crystal to maximize total laser power.

7. Because of the fact that different wavelengths diffract differently passing through the semi transparent mirror (3) and the crystal the angles of the cavity ends (output coupler and grating) has to be manually corrected when scanning over a larger wavelength interval to keep the two cavities in sync.

4.8 Data collection

Neutral particle detections were accumulated for 15 detection rounds for every element (O^-, Ag^-, PdO^- and AgO^-) for every wavelength investigated. Average values of the detection counts, corresponding ion beam current in the last Faraday cup and measured laser power were plotted against the photon energy of the laser (conversion to photon energy in eV from laser beam wavelength, $E = hc/\lambda$). Background detections (window B in figure 20) were subtracted from the photodetachment detection counts for each round and the estimated isolated/pure photodetachment detections were normalized with respect to laser power and ion beam current. Maximum, minimum and average values were extracted and plotted against photon energy to visualize the photodetachment behaviours. To estimate the relative photodetachment cross section difference between AgO^- and PdO^- their normalized counts are divided by the normalized counts for Ag^- and the results are plotted against photon energy. A mass scan was also performed by measuring the current in the last Faraday cup while increasing the supply current for the bending magnet.

5 Proof of principle measurements O^-

The motivation behind the O^- measurement is to show that we can replicate the already known photodetachment cross section behaviour of O^- to give us confidence that our other results can be trusted and conclusions can be drawn from them.

Figure 22 shows the neutral particle counts accumulated in the photodetachment window (window A) for the different photon energies investigated (approximately 1,42 eV to 1,51 eV). In figure 23 you can see a log plot visualizing a satisfactory signal to noise ratio and in figure 24 you see the ion beam current and measured laser power. Comparing figure 22 and 24 you can clearly spot the correlation between laser power and neutral particle counts. This is a clear indication about the necessity of normalization with respect to laser power.

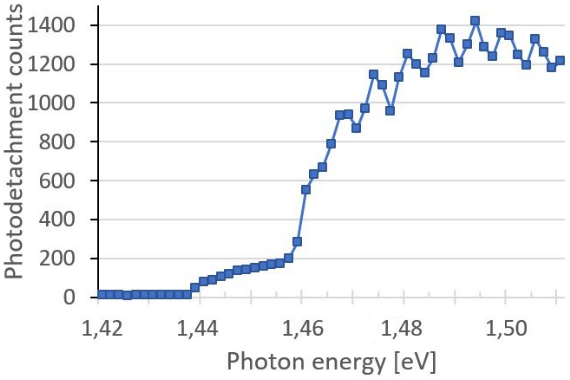

Figure 22: *Photodetachment counts* O^-

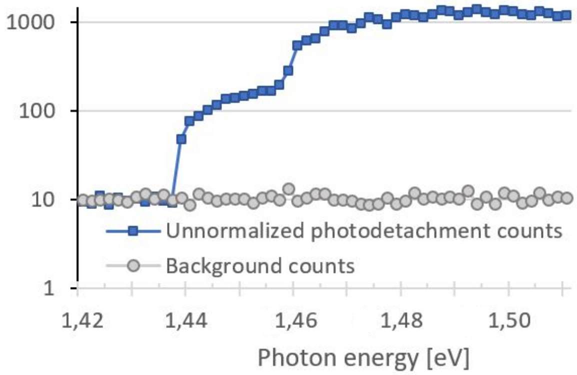

Figure 23: *Logarithmic plot of the neutral particle counts*

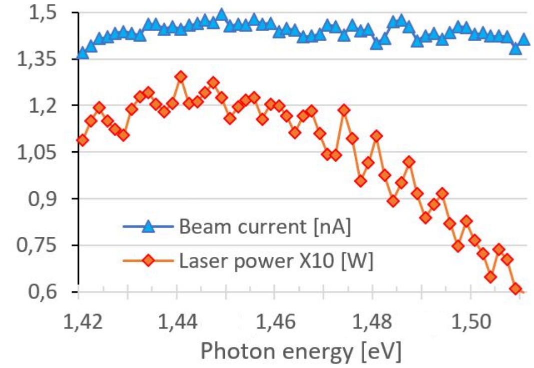

Figure 24: *Ion beam current and laser power*

The intensity oscillations observed in both figure 22 and 24 is most likely produced by a Fabry-Perot effect inside the laser setup. If you have two parallel semi-transparent surfaces you will have light bouncing back and fourth between the surfaces. Depending on the width between the surfaces (d), the incoming angle (α) and wavelength (λ) of the light, the transmissions from light that has bounced different amount of times will either add their intensities or cancel each other out. Maximum intensity is reached when the relation in equation 7 is fulfilled [31].

$$2d\ \cos\alpha = m\ \lambda \tag{7}$$

Measuring the wavelength difference between two peaks in the ”zig-zag” / saw-tooth pattern in figure 24 yields information about the distance between the parallel surfaces in the laser setup that produced the effect.

In figure 25 you can see the plot of the normalized photodetachment counts calculated by equation 8.

$$Normalized\ counts = \frac{Photodetachment\ window\ counts - Background\ window\ counts}{Ion\ beam\ current * Laser\ power} \tag{8}$$

Figure 26 shows the logarithmic plot of the same results making it possible to visualize another perspective, and compare it to the apparent increase in the size of the error bars with higher photon energy in figure 25. This apparent increase is most likely caused by the classic statistical behaviour of a Poisson distribution. With higher photon energies you would see a greater integer deviation in accumulated counts because of the fact that you simply have a greater mean amount. However, you will by the same logic have a smaller relative error with higher photon energies (in percent), as is somewhat visualized in the log-plot in figure 26.

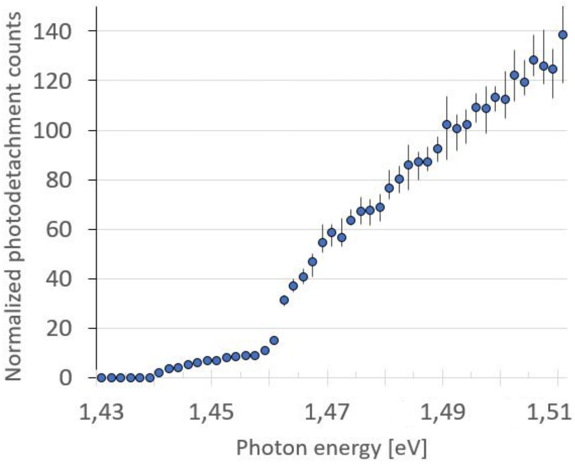

Figure 25: *Normalized photodetachment counts O$^-$*

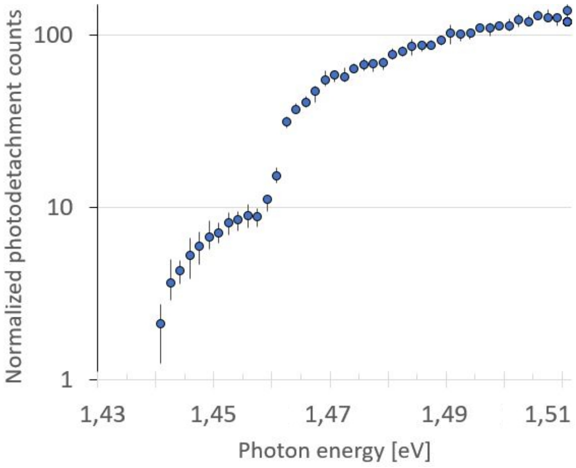

Figure 26: *Logarithmic plot of the normalized photodetachment counts O$^-$*

Figure 27 shows the normalized counts of photo-neutralized oxygen with an added sketched cross section curve estimated from earlier experimental results and theoretical modeling of the cross section behaviour of O$^-$ [20][21]. Comparing figure 27 to figure 2 in the introduction we can see that GUNILLA is capable of producing satisfactory laser photodetachment threshold spectroscopy results. This gives us the opportunity of obtaining reliable estimates of electron affinities and a general grasp of laser photodetachment behaviours. The results are also precise enough to somewhat visualize the fine structure splitting in the energy levels of O$^-$ discussed in the background chapter.

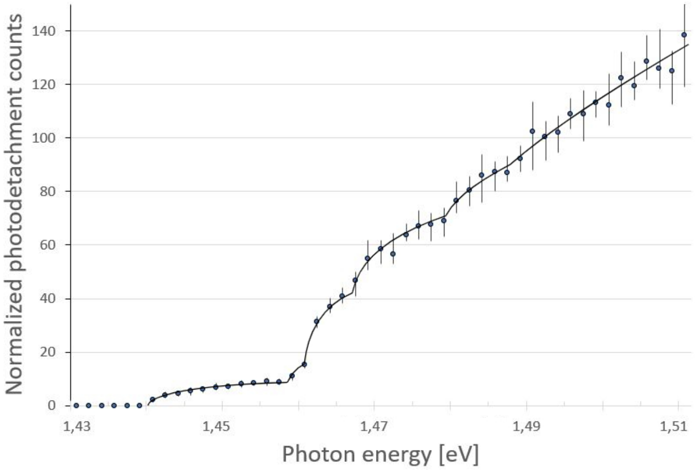

Figure 27: *Normalized detection counts O$^-$ (dots with error bars) and estimated cross section behaviour (solid line).*

6 Results Ag^-, AgO^- and PdO^-

In figure 28 you can see the result of the mass scan performed in the Ag to PdO_2 mass interval visualizing the relevant contents of the sample. It also yields the relative ion beam production rate for the different elements (height of peaks $\propto$ ion beam current) accelerated from the 50/50 AgO^-/PdO^- mixture powder described in chapter 3. The photodetachment measurements were performed on the ^{107}Ag, ^{123}AgO and ^{124}PdO peaks.

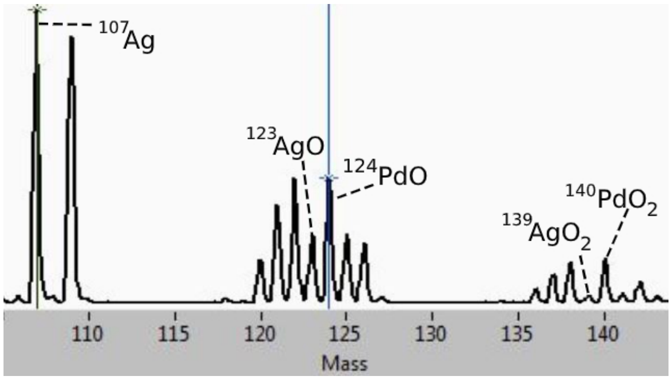

Figure 28: *Mass scan*

Figure 29 shows the detection counts for the photodetachment window and figure 30 the measured background counts. In figure 31 you can see the ion beam current measured in the last Faraday cup and in figure 32 the measured laser power (all plotted against investigated photon energy).

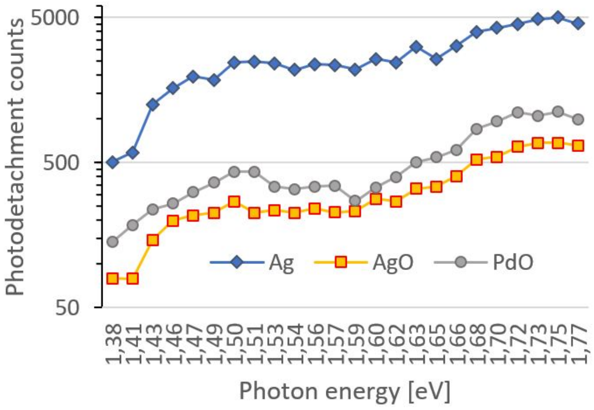

Figure 29: *Unnormalized photodetachment detection counts*

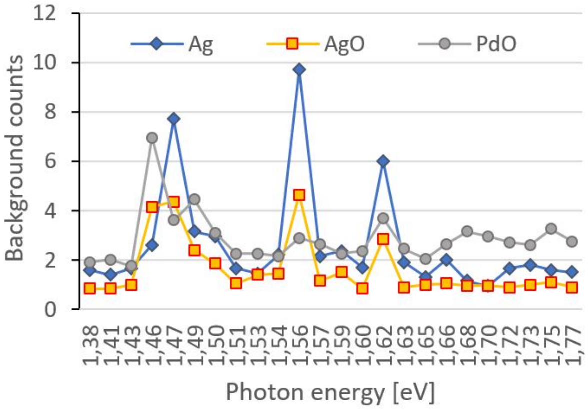

Figure 30: *Background detection counts*

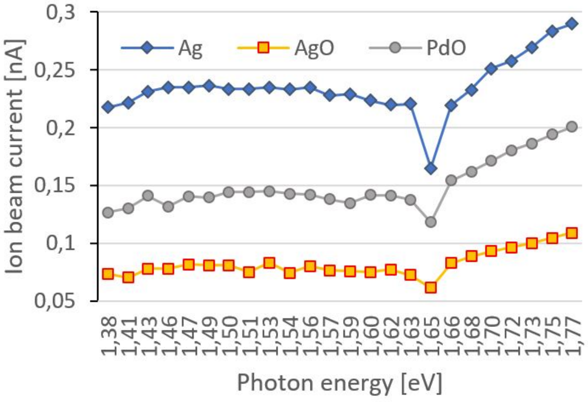

Figure 31: *Ion beam current*

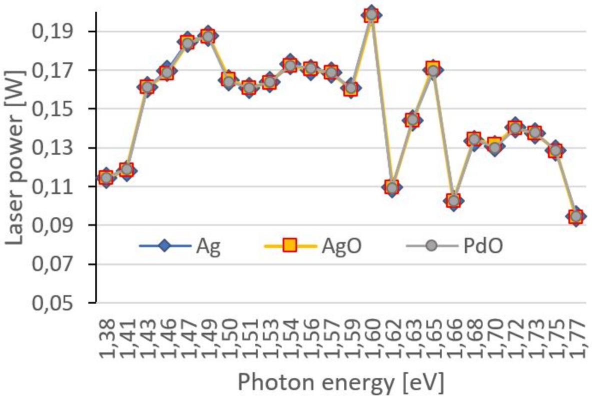

Figure 32: *Laser power*

Figure 33 and 34 shows the normalized counts (calculated with eq 8) for Ag, AgO and PdO. Figure 35 shows the measured relative photodetachment cross sections for AgO^- and PdO^- in relation to Ag^- with fitted 3rd order polynomials visualizing the trend in relation to photon energy.

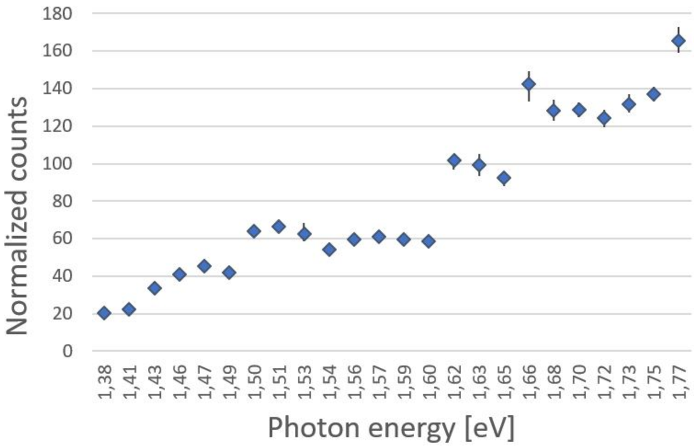

Figure 33: *Normalized counts* Ag

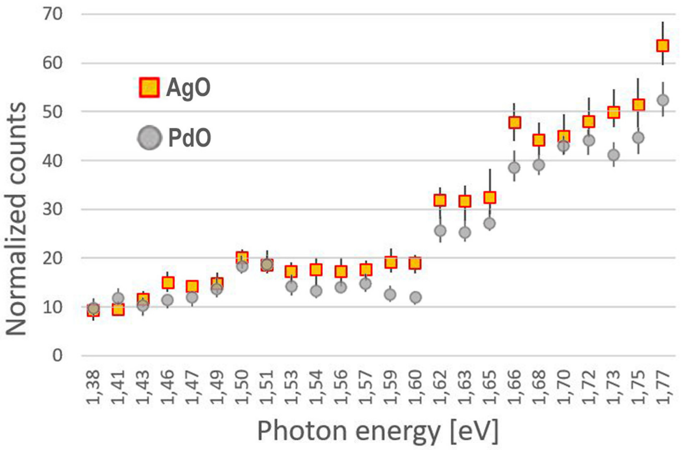

Figure 34: *Normalized counts* Ago *and* PdO

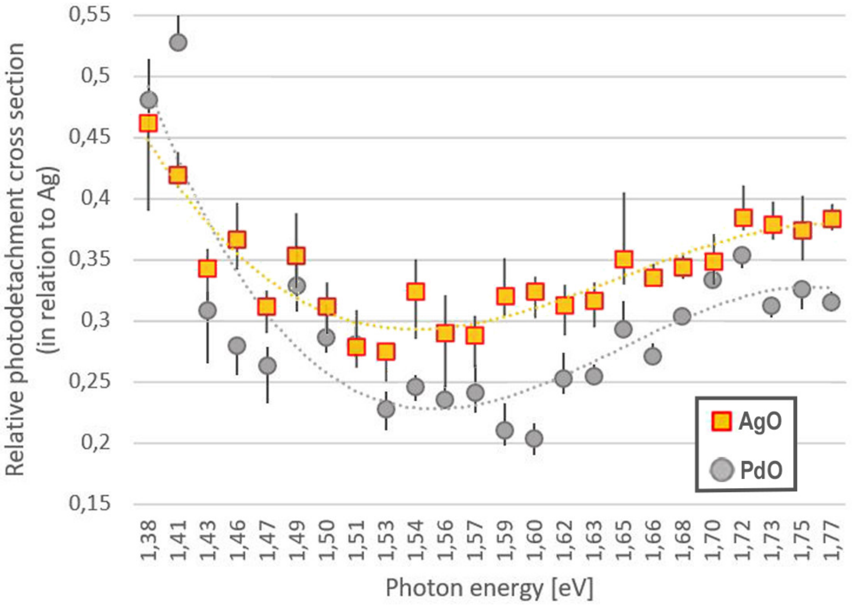

Figure 35: *Relative photodetachmnet cross section in relation to Ag. Dotted lines are 3rd order polynomials fitted to the measured data.*

7 Discussion

7.1 Normalization

From the photodetachment measurement results gathered for Ag^-, AgO^- and PdO^- we can see a clear example of why normalization to not only laser power but also ion beam current is critically important. This normalization is vital to counteract the observed ion beam fluctuations and differences in ion beam intensity between the elements. You can, when comparing unnormalized with normalized photodetachment counts (figure 29 and 34), see that the order of the elements (which element that has the highest amount of counts) is not the same (looking at AgO and PdO). This clearly has to do with the difference in ion beam intensity for the two elements (figure 31).

7.2 Laser calibration and probable laser beam overlap issues

For the Ag^-, AgO^- and PdO^- measurements we performed a manual step-by-step scan with larger steps (compared to the oxygen measurements). The investigated step-by-step photon energies are specified on the x-axis of figure 29-35 and can be compared to the semi-continuous scan performed by a computer program in the O^- measurement (figure 22-27). When performing a scan over a larger wavelength interval the laser cavities had to be recalibrated at certain wavelengths (as mentioned in chapter 4.7). This was easier to do if you directly could observe that the cavities came out of sync (partial loss in laser power) when performing a manual step-by step-change of wavelength/photon energy. If an automated larger interval scan had been run by a computer program you would at some wavelength lose all laser power and be forced to manually calibrate the laser (harder to do without any initial laser power to guide you) and redo the measurement anyway.

In figure 33 and 34 you can see some discontinuities (”jumps”) in the curves that coincide with the performed cavity calibrations mentioned above. These are probably caused by a small initially unnoticed change, that we later could observe (see figure 57 appendix A.3), in the direction of the laser beam caused by the calibration. This is reasonable since we change the angles of the mirrors when calibrating the cavities and thereby probably change the output angle. This could in turn affect the overlap of the laser beam and ion beam and cause the observed discontinuity behaviour.

The observed discontinuity problem is probably somewhat neglectable when, as is the focus of this project, investigating the differences in photodetachment cross section behaviour between AgO^- and PdO^-. If the jump behaviour in figure 33 and 34 originates from changing the laser system and we change between elements before changing laser wavelength we would have approximately the same overlap issues for AgO^- and PdO^-. This assumes that the ion beam position/direction is approximately the same for at least AgO^- and PdO^- (since they are close in mass). This assumption is defended by the fact that we do not see the jumps to the same extent in figure 35 and the jumps are approximately the same percentile for the different elements.

Some considerations should be made about possible overlap issues when extracting absolute photodetachment cross section values from the relative values received in this project. We can not conclude that the overlap is exactly the same for Ag^- and the oxides since there is a somewhat significant mass difference. This could affect the exactness of the values on the y-axis in figure 35.

7.3 Mass scan: thoughts on possible contaminations

For the AgO and PdO mesurments we concluded that for the measured peaks (mass 123 and 124) we could identify the element by looking at the isotope abundances of Ag and Pd. We concluded that the peak with mass 123 corresponded to ^{107}Ag with an oxygen atom attached and the peak with mass 124 was the palladium isotope ^{108}Pd with an oxygen atom attached. We also performed a fast test to confirm that we did not have hydride contaminations by comparing the normalized photodetachment counts for the different isotopes close to the top of the peaks in the mass scan. The normalized photodetachment count should be the same for isotopes of the same element and be fairly stable near the peak tops. If we would have contaminations (i.e. hydrides) with approximately the same mass as the isotope we are looking at we would see deviations from the mean normalized photodetachment counts of that element when scanning/ choosing a magnet current slightly different than the peak top (hitting a contaminant). No such deviations were observed. The conclusion that no hydride contaminations were present was also backed up by looking at the relations between the oxide peaks and their estimated abundances and also how many oxide peaks you would estimate to have, compared to how many you observe. If you would have one more peak to the right of the last estimated observable isotope, and the beam current relations between the first and the second isotope differs from the estimated abundances, that would correspond to having a possible hydride contamination. No such behaviour was observed.

You could also speculate that even if you had some hydride contaminations that went unnoticed the fact that those molecules would be slightly larger and possible more polarizable means that their electron affinities probably would be higher than the oxides. This is maybe an unnecessary speculation but gives extra confidence as a second hypothetical backup, since they probably still would be negatively charged in the investigated laser energy range.

7.4 Background detection

If you look at figure 30 (the background detections) you can see a few spikes that seem to be correlated for the different elements. These were likely caused by the quadrupole deflector. It occasionally discharged (measurable current from the electrodes) and we observed that this was correlated to the amount of measured background detections. This additional background may come from free electrons created by the discharging electrodes that could interact/collide with the ion beam and create stray particles that reach the detector. The fact that it seems to be correlated with laser beam frequency also points to this since we measured the elements one after the other in a reasonable short time period (which could coincide with an unoticed quadrupole discharging ”episode”) before changing laser wavelength. The discharge was at times so bad that we had to shut down the quadrupole deflector, wait a couple of minutes and start it up again to redo the measurements for that specific wavelength. This was another factor explaining why we had so much fewer data points measuring on Ag^-, AgO^- and PdO^- compared to the oxygen measurements.

7.5 Ion beam current

In figure 31 you can see a dip in the ion beam current for all the elements at a certain laser wavelength. This dip is probably either caused by grounding problems with some component along the beam line or the cesium sputter source. It could have to do with the fact that we manually change between the elements by varying the bending magnet current to hit a top of the peak (figure 28) when investigating a certain laser wavelength (one element after the other as mentioned above). However this seems unlikely since it suddenly seems to happen for all three elements at a certain laser wavelength and not at the other wavelengths. It is more likely that this behaviour has to do with the source or some other component since we during the project had serious and regularly occurring beam instability problems. At its worst the experimental setup was completely unusable since the ion beam current was too unstable, with rapid fluctuations in beam intensity over short time intervals (too fast changes to successfully monitor and combat with normalisation). The fluctuation in ion beam intensity is visualized in figure 36.

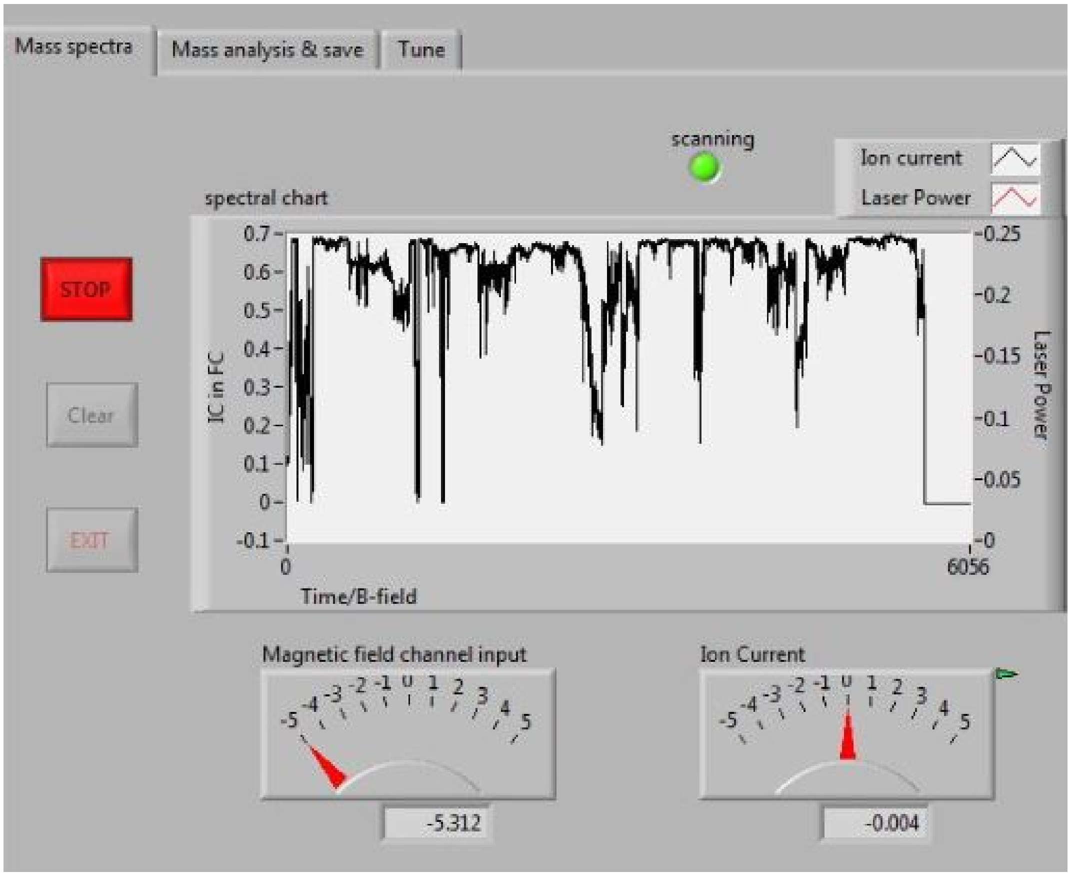

Magnetic field channel input -5.312

Ion Current -0.004

Figure 36: *Snapshot of the labVIEW control program for GUNILLA visualizing ion beam intensity fluctuations. Area of interest is the chaotic fluctuations inside the "spectral chart" window visualizing ion beam current in nA over time.*

The chaotic behaviour seen in the "spectral chart" vindow (optimally this should be a somewhat straight line at a certain ion beam current) was indicative of the regularly observed ion beam instability behaviour. During the performed measurements no such quick unnormalizable fluctuations was observed and the results visualized in figure 31 can therefore be trusted.

8 Conclusion

The data from the measurements on Ag^-, AgO^- and PdO^- could definitely have been improved (overlap, smoother graphs etc.) but with the accuracy of the O^- measurements in mind we concluded that they were sufficiently accurate for the overall purpose of the experiment. In other words, the problems that occurred did not greatly affect the goal of the project: to investigate if AgO^- and PdO^- are suitable candidates for selective laser photodetachment suppression of ^{107}Ag with regards to ^{107}Pd.

From the general cross section behaviors observed in figures 33-35, we can clearly see that the curve of PdO^- follows the curve of AgO^- in such a way that it, in the investigated photon-energy range, makes selective laser photodetachment suppression of AgO^- impossible. There is no photon energy where photodetachment of AgO^- is possible without having a rather large probability of also detaching electrons from PdO^- (which clearly defeats the purpose of selective laser photodetachment suppression in AMS).

We can therefore conclude that the anionic oxides are unsuitable candidates for selective laser photodetachment suppression of ^{107}Ag in AMS ultra trace abundance measurements of ^{107}Pd.

8.1 Extentions and future work

A general extension comment is that future LPTS projects at GUNILLA should correct the problems discussed in chapter 7. Examples of such corrections could be to install a beam scanner to monitor ion beam/laser beam overlap or performing a laser system upgrade to automatically correct variations in laser output direction (the ion beam instability problems was more or less solved in this project by the rigorous troubleshooting of GUNILLA mentioned in the preface).

It could, in relation to this specific experimental project, be interesting to look at both a smaller laser frequency interval (idealy with ion beam cooling) around the earlier estimated electron affinity values and at a larger laser frequency interval. It would be interesting to see what happens at higher energies (not just the estimated EA interval) and also when the normalized photodetachmnent detections drop down to zero. A lot of the neutral particle detections in the lower energy range probably comes from photodetachments from vibrational exited states. Scanning the laser frequency over a larger range could perhaps shed some further light on this behaviour. A more detailed look in the vicinity of the earlier estimated electron affinities, with a cold beam, could suppress possible vibrational blurring of differences in photodetachment behaviour between the elements. The observed differences in this project are however so small that it is unlikely that it would change the conclusion, since the desired application is suppression of a highly abundant contaminant in ultra trace measurements. All of the extentions of the experiment mentioned would likely not give any extra insights relevant to the goal of investigating selective laser photodetachment posibilities of AgO^-. It remains likely that the oxides are unsuitable candidates.

A logical next step in the search for a suitable molecular system, proposed with the results from this project in mind, would be to compare the cross section behaviours of the dioxides ($AgO_2{}^-$ and $PdO_2{}^-$). The differences we see in photodetachment cross section behaviour of the oxides could be pronounced in the dioxides since the binding energy of the extra electron probably would be greater (larger more polarizable molecules). It could also be that there are some differences in the superhalogenic properties of $AgO_2{}^-$ and $PdO_2{}^-$ [32] that would make the photodetachment cross section differences sufficiently pronounced. One result from this project pointing to the possibility of the dioxides being a suitable molecular system is the peak height differences between AgO_2^- and PdO_2^- observed in figure 28. The bigger differences between the peaks for the dioxides compared to the oxides could be an indication of a bigger difference in the electron affinties (the production rate is generally correlated to the electron affinity [33]).

Other molecular candidates for selective laser photodetachment suppression of ^{107}Ag to be experimentally investigated, if the dioxides also turn out to be unsuccessful, are the fluorides. If the fluorides are also unsuitable for selective laser photodetachment suppression of silver, the next step would be an exhaustive, iterative search over all possible molecular candidates. You would keep on working your way through the periodic table looking for molecular candidates until you either find a suitable system or run out of elements. A comment should be made here about the earlier mentioned emphasis on ”easily produced molecular systems”. An unsuitable candidate would also be one that is unreasonably expensive to produce or investigate. Applied experimental physics lives in the real world and is therefore inherently practical.

References

[1] G. Quarta, S. Malgora, M. D'Elia, V. Gaballo, E. Braione, L. Maruccio, C. Corvaglia, and L. Calcagnile. The strange case of the ankhpakhered mummy: Results of ams 14 c dating. *Radiocarbon*, 55(2-3):1403–1408, 2013.

[2] J. R. Richards. Age of the earth's crust and lead model ages. *Nature*, 195(4836):65, 1962.

[3] L K Fifield. Accelerator mass spectrometry and its applications. *Reports on Progress in Physics*, 62(8):1223–1274, 1999.

[4] A. Wallner, J. Feige, N. Kinoshita, M. Paul, L. K. Fifield, R. Golser, M. Honda, U. Linnemann, H. Matsuzaki, S. Merchel, G. Rugel, S. G. Tims, P. Steier, T. Yamagata, and S. R. Winkler. Recent near-earth supernovae probed by global deposition of interstellar radioactive 60fe. *Nature*, 532(7597):69, 2016.

[5] J. van der Plicht. Radiocarbon dating | variations in atmospheric 14c. In *Encyclopedia of Quaternary Science*, pages 2923–2931. 2007.

[6] G. S. Burr. Radiocarbon dating; causes of temporal variations. In *Encyclopedia of Quaternary science; Volume 4*, pages 2931–2941. Elsevier, Amsterdam, 2007.

[7] G.T. Cook and J. van der Plicht. Radiocarbon dating | conventional method. In *Encyclopedia of Quaternary Science*, pages 2899–2911. 2007.

[8] W. Kutschera. Applications of accelerator mass spectrometry. *International Journal of Mass Spectrometry*, 349-350(1), 2013.

[9] A.J.T. Jull. Radiocarbon dating | ams method. In *Encyclopedia of Quaternary Science*, pages 2911–2918. 2007.

[10] Walter Kutschera. Progress in isotope analysis at ultra-trace level by ams. *International Journal of Mass Spectrometry*, 242(2):145–160, 2005.

[11] Pontus Andersson. *Laser photodetachment of negative ions : fundamental research and applications*. Department of Physics, University of Gothenburg, Göteborg, 2009.

[12] Martin Martschini, Dag Hanstorp, Johannes Lachner, Christoph Marek, Alfred Priller, Peter Steier, Paul Wasserburger, and Robin Golser. The iliams project – an rfq ion beam cooler for selective laser photodetachment at vera. *Nuclear Inst. and Methods in Physics Research, B*, 456:213–217, 2019.

[13] H.-A. Synal. Developments in accelerator mass spectrometry. *International Journal of Mass Spectrometry*, 349-350(1), 2013.

[14] Martin Martschini, Johanna Pitters, Tobias Moreau, Pontus Andersson, Oliver Forstner, Dag Hanstorp, Johannes Lachner, Yuan Liu, Alfred Priller, Peter Steier, and Robin Golser. Selective laser photodetachment of intense atomic and molecular negative ion beams with the ilias rfq ion beam cooler. *International Journal of Mass Spectrometry*, 415:9–17, 2017.

[15] R.C. Bilodeau, M. Scheer, and H.K. Haugen. Infrared laser photodetachment of transition metal negative ions: Studies on cr - , mo - , cu - and ag -. *Journal of Physics B: Atomic, Molecular and Optical Physics*, 31(17):3885–3891, 1998.

[16] Michael Scheer, Cicely A. Brodie, René C. Bilodeau, and Harold K. Haugen. Laser spectroscopic measurements of binding energies and fine-structure splittings of co , ni , rh , and pd . *Physical Review A*, 58(3):2051–2062, 1998.

[17] Tanya Ramond, Gustavo Davico, Fredrik Hellberg, Fredrik Svedberg, P. Salen, Patrick Söderqvist, and W. Lineberger. Photoelectron spectroscopy of nickel, palladium, and platinum oxide anions. *Journal of Molecular Spectroscopy - J MOL SPECTROSC*, 216:1–14, 11 2002.

[18] Django Andrews, Adam Gianola, and W. Lineberger. On the photoelectron spectrum of ago. *The Journal of Chemical Physics*, 117:4074–4076, 08 2002.

[19] Dag Hanstorp and David Pegg. *Photodetachment - chapter 60 in the Springer Handbook of Atomic, Molecular, and Optical Physics, 2nd edition*. 07 2020(in press).

[20] Lewis M. Branscomb, David S. Burch, Stephen J. Smith, and Sydney Geltman. Photodetachment cross section and the electron affinity of atomic oxygen. *Phys. Rev.*, 111:504–513, Jul 1958.

[21] Gregory Miecznik and Chris Greene. Calculation of near-threshold o- photodetachment, including fine-structure effects. *Physical review. A*, 53:3247–3252, 06 1996.

[22] J. Chen and G. Wasserburg. The isotopic composition of ag in meteorites and the presence of pd107 in protoplanets. *Geochimica Et Cosmochimica Acta - GEOCHIM COSMOCHIM ACTA*, 54:1729–1743, 06 1990.

[23] William Kelly and G. Wasserburg. Evidence for the existence of 107pd in the early solar system. *Geophysical Research Letters*, 5, 12 1978.

[24] Maximilian Matthes, M. Fischer-Gödde, Thomas Kruijer, Ingo Leya, and Thorsten Kleine. Pd-ag chronometry of iron meteorites: Correction of neutron capture-effects and application to the cooling history of differentiated protoplanets. *Geochimica et Cosmochimica Acta*, 10 2015.

[25] R. Middleton. A review of ion sources for accelerator mass spectrometry. *Nuclear Instruments and Methods in Physics Research Section B: Beam Interactions with Materials and Atoms*, 5(2):193 – 199, 1984.

[26] Infopage-Helmholtz institute for ion beam phyics and material reaserch. Impatient scientists: Accelerator mass spectrometry (ams) for the determination of long-lived radionuclides. *https://www.hzdr.de/db/cms?POid=27781pNid=1061SP*", 05 2020.

[27] Wan Hong, Jung Hun Park, Kyeong J Kim, Hyung Joo Woo, Jun Kon Kim, Han Woo Choi, and Gi Dong Kim. Establishment of chemical preparation methods and development of an automated reduction system for ams sample preparation at kigam. *Radiocarbon*, 52(3):1277–1287, 2010.

[28] C P Kohl and K Nishiizumi. Chemical isolation of quartz for measurement of in-situ-produced cosmogenic nuclides. *Geochimica et Cosmochimica Acta; (United States)*.

[29] C. Vockenhuber, Andreas Bergmaier, Thomas Faestermann, Klaus Knie, Gunther Korschinek, W. Kutschera, Georg Rugel, Peter Steier, K. Vorderwinkler, and Anton Wallner. Development of isobar separation for 182hf ams measurements of astrophysical interest. *Nuclear Instruments and Methods in Physics Research Section B: Beam Interactions with Materials and Atoms*, 259:250–255, 06 2007.

[30] Ursel Fantz, R Friedl, and Markus Froeschle. Controllable evaporation of cesium from a dispenser oven. *The Review of scientific instruments*, 83:123305, 12 2012.

[31] Hyperphysics.edu. Fabry-perot geometry. *http://hyperphysics.phy-astr.gsu.edu/hbase/phyopt/fabry.html*, 05 2020.

[32] Ambrish K. Srivastava and Neeraj Misra. Theoretical investigations on the superhalogen properties and interaction of pdon (n=1-5) species. *International Journal of Quantum Chemistry*, 114, 03 2014.

[33] Roy Middleton. *A negative ion cookbook*. 10 1989.

A Appendix

A.1 Controls

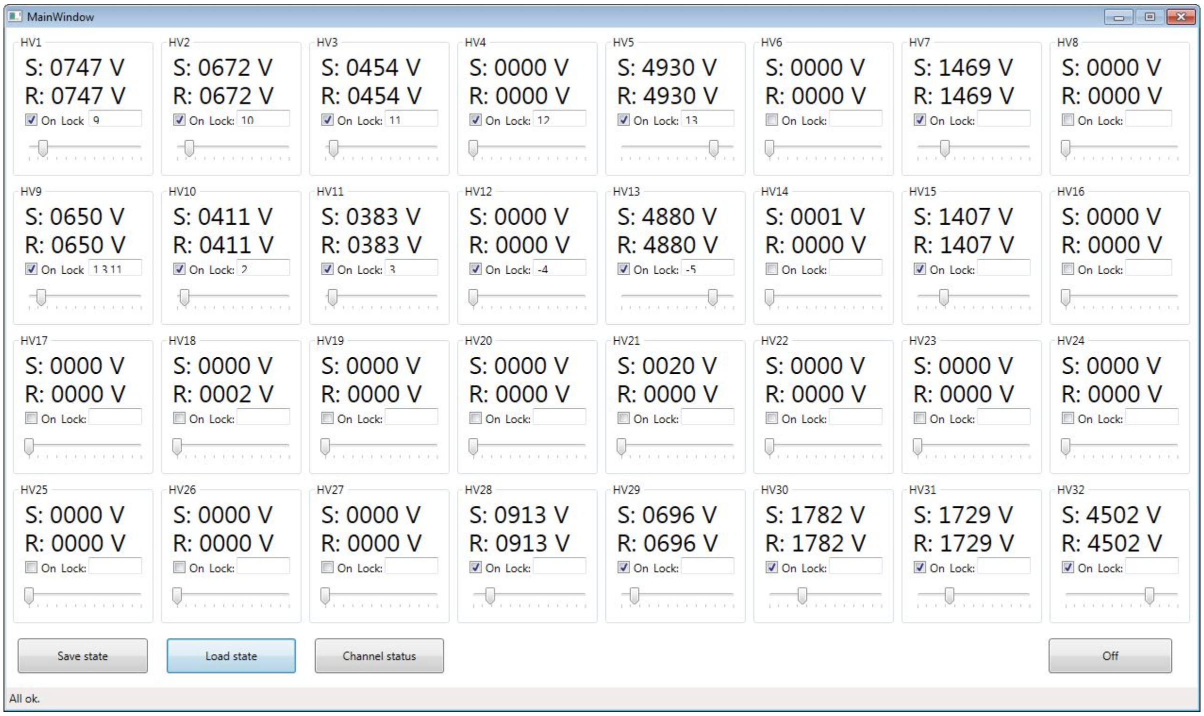

HV1
S: 0747 V
R: 0747 V
☑ On Lock 9

HV2
S: 0672 V
R: 0672 V
☑ On Lock: 10

HV3
S: 0454 V
R: 0454 V
☑ On Lock: 11

HV4
S: 0000 V
R: 0000 V
☑ On Lock: 12

HV5
S: 4930 V
R: 4930 V
☑ On Lock: 13

HV6
S: 0000 V
R: 0000 V
☐ On Lock:

HV7
S: 1469 V
R: 1469 V
☑ On Lock:

HV8
S: 0000 V
R: 0000 V
☐ On Lock:

HV9
S: 0650 V
R: 0650 V
☑ On Lock 1,3,11

HV10
S: 0411 V
R: 0411 V
☑ On Lock: 2

HV11
S: 0383 V
R: 0383 V
☑ On Lock: 3

HV12
S: 0000 V
R: 0000 V
☑ On Lock: -4

HV13
S: 4880 V
R: 4880 V
☑ On Lock: -5

HV14
S: 0001 V
R: 0000 V
☐ On Lock:

HV15
S: 1407 V
R: 1407 V
☑ On Lock:

HV16
S: 0000 V
R: 0000 V
☐ On Lock:

HV17
S: 0000 V
R: 0000 V
☐ On Lock:

HV18
S: 0000 V
R: 0002 V
☐ On Lock:

HV19
S: 0000 V
R: 0000 V
☐ On Lock:

HV20
S: 0000 V
R: 0000 V
☐ On Lock:

HV21
S: 0020 V
R: 0000 V
☐ On Lock:

HV22
S: 0000 V
R: 0000 V
☐ On Lock:

HV23
S: 0000 V
R: 0000 V
☐ On Lock:

HV24
S: 0000 V
R: 0000 V
☐ On Lock:

HV25
S: 0000 V
R: 0000 V
☐ On Lock:

HV26
S: 0000 V
R: 0000 V
☐ On Lock:

HV27
S: 0000 V
R: 0000 V
☐ On Lock:

HV28
S: 0913 V
R: 0913 V
☑ On Lock:

HV29
S: 0696 V
R: 0696 V
☑ On Lock:

HV30
S: 1782 V
R: 1782 V
☑ On Lock:

HV31
S: 1729 V
R: 1729 V
☑ On Lock:

HV32
S: 4502 V
R: 4502 V
☑ On Lock:

All ok.

Figure 37: *Layout control program high voltage ion optics(HV 1 upper left HV 32 lower right). HV 32=einzel lens, HV 30-31 =x-lens,HV 28-29 =y-lens, HV 1-3 o 9-11=quadrupole triplet lens, HV 5 o 13= quadrupole deflector and HV 7 o 15=deflector FC3.*

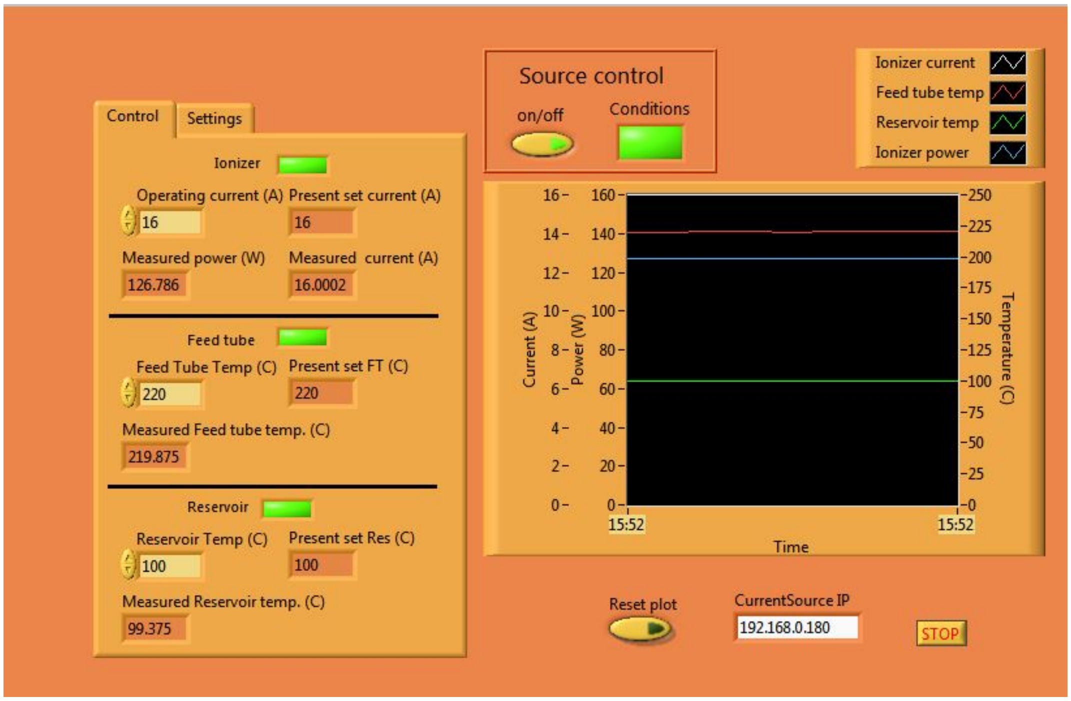

Ionizer

Operating current (A) 16

Present set current (A) 16

Measured power (W) 126.786

Measured current (A) 16.0002

Feed tube

Feed Tube Temp (C) 220

Present set FT (C) 220

Measured Feed tube temp. (C) 219.875

Reservoir

Reservoir Temp (C) 100

Present set Res (C) 100

Measured Reservoir temp. (C) 99.375

CurrentSource IP 192.168.0.180

Figure 38: *Layout of LabVIEW control program source*

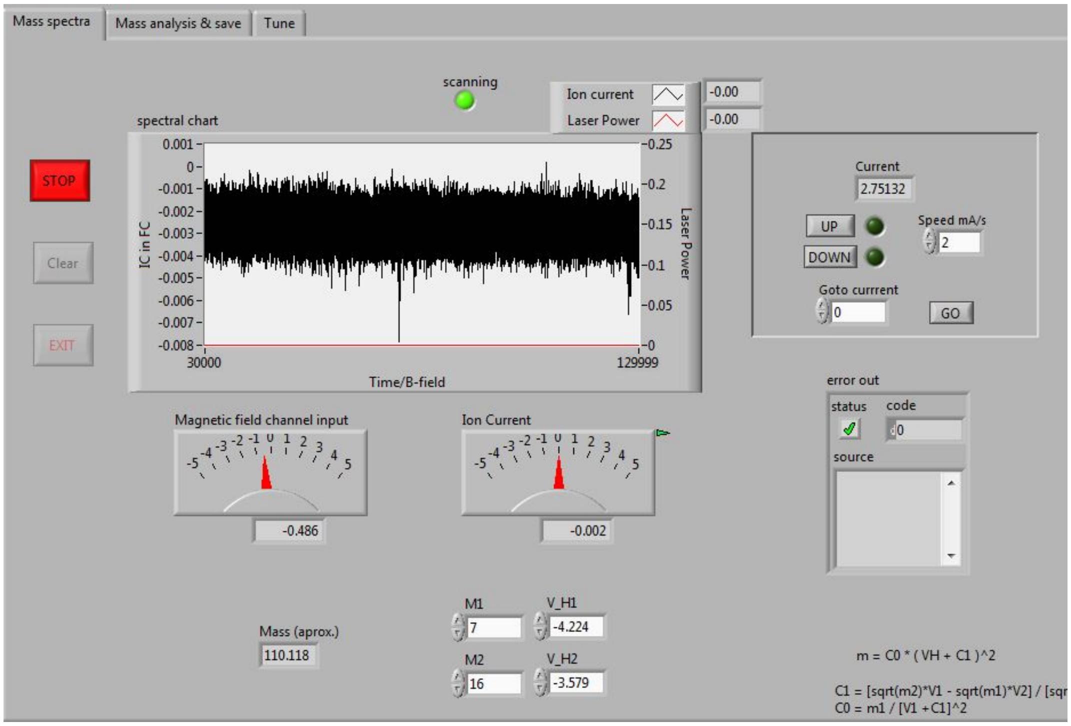

Ion current -0.00

Laser Power -0.00

Current 2.75132

Speed mA/s 2

Goto currrent 0

error out

status ✓ code 0

source

Magnetic field channel input -0.486

Ion Current -0.002

Mass (aprox.) 110.118

M1 7

V_H1 -4.224

M2 16

V_H2 -3.579

m = C0 * (VH + C1)^2

C1 = [sqrt(m2)*V1 - sqrt(m1)*V2] / [sqr

C0 = m1 / [V1 +C1]^2

Figure 39: *Layout of the LabVIEW control program for the bending magnet and ion beam current measurements. Current selection for the magnet on the right, beam current readout from selected Faraday-cup in the middle "spectral chart" -window and mass calibration for magnet current below.*

A.2 Experimental setup preparation

1. **Cathode preparation and source setup:** After preparing the cathode (drilling/filling with powder) a written step by step instruction for changing of the cathode was followed. The main points has to do with grounding high voltage components for safety reasons and closing off the rest of the beam line so that there will be no vacuum problem when you remove/insert the cathode rod. After this the power supplies for the acceleration are turned on and the source is started from the control program (figure 38). A warm up time of approximately 90 min is needed before the source has somewhat stabilized.

2. **Initial optimisation of the ion beam** After the source has warmed up you can start the ion optics program and optimise the beam current in the first Faraday cup by changing the voltages on the electrodes of the einzel lenz and x-lens (figure 37).

3. **Bending magnet and further optimization** The next step is to calibrate the bending magnet. This is quite easily done by selecting the second Faraday cup and scaning the magnet (increasing the current passing through the magnet from zero and upward) and identifying two peaks to use as calibration points. Usually oxygen is used as the first peak as it is distinct and pops up quite early in the mass scan (mass 16). The other peak can for example be one of the oxide peaks of silver or palladium you later want to isolate (the shape of the oxide bunch is quite distinct as can be seen in the results section). After this you choose the first element you want to investigate and optimise the beam again (now in Faraday cup 2) with all the optical components up to Faraday cup 2. Then you select the Faraday cup after the interaction region and optimize the beam again including the last optical components. Here you can as mentioned earlier use the first collimator plate to get initial information on the direction of the beam after the quadrupole deflector. For the investigations of Ag, AgO and PdO you optimize the beam for Ag and keep the settings for the two other elements so that you get as little deviation as possible in the overlap with the laser (since you want to compare the results).

4. **Setup and continuous adjustment of the TISA laser:** The Nd:Yag laser needs approximately 20 minutes to warm up and stabilize before the beam is let into the Ti:Sa laser chamber (figure 21). For the oxygen measurement the wavelength interval was small enough so that the two cavities did not need readjustments (as mentioned in point 7 of the laser description section) during the oxygen measurements a computer program was used to perform a semi-continuous scan (to get more detailed data) over the wanted wavelength interval (816 nm - 870 nm). For the other three elements a cavity readjustment was needed at certain wavelength points during the scan which made the use of the previously mentioned scan program difficult. As a result fewer data points further apart was collected, compared to the oxygen scan (as mentioned in the chapter 7).

A.3 Documentation pictures

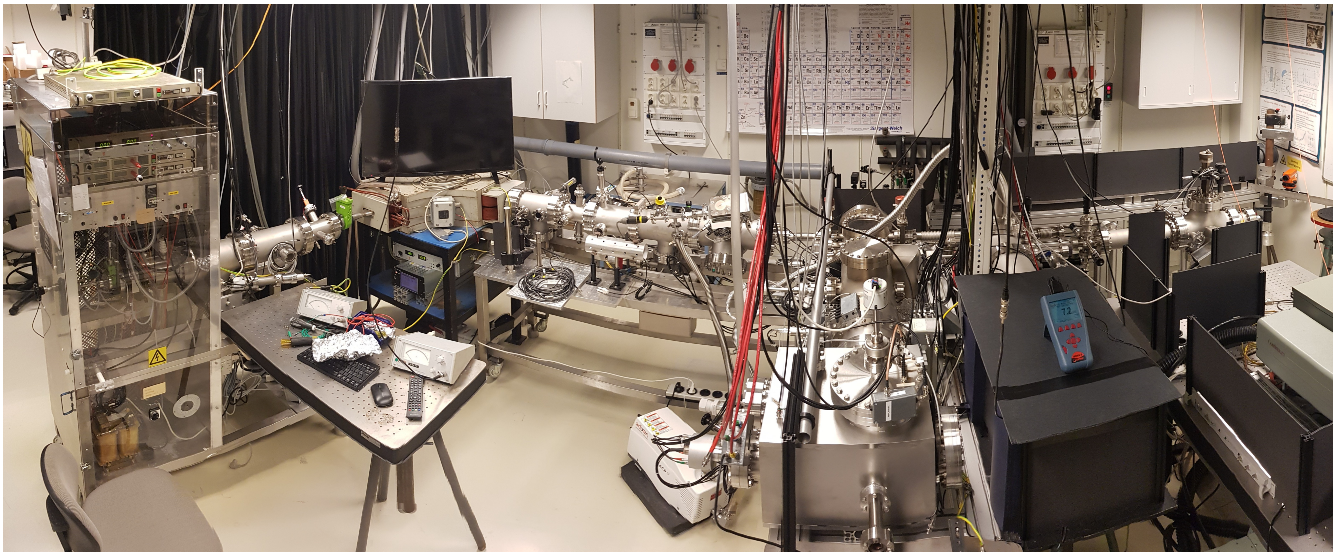

Figure 40: *Overview GUNILLA*

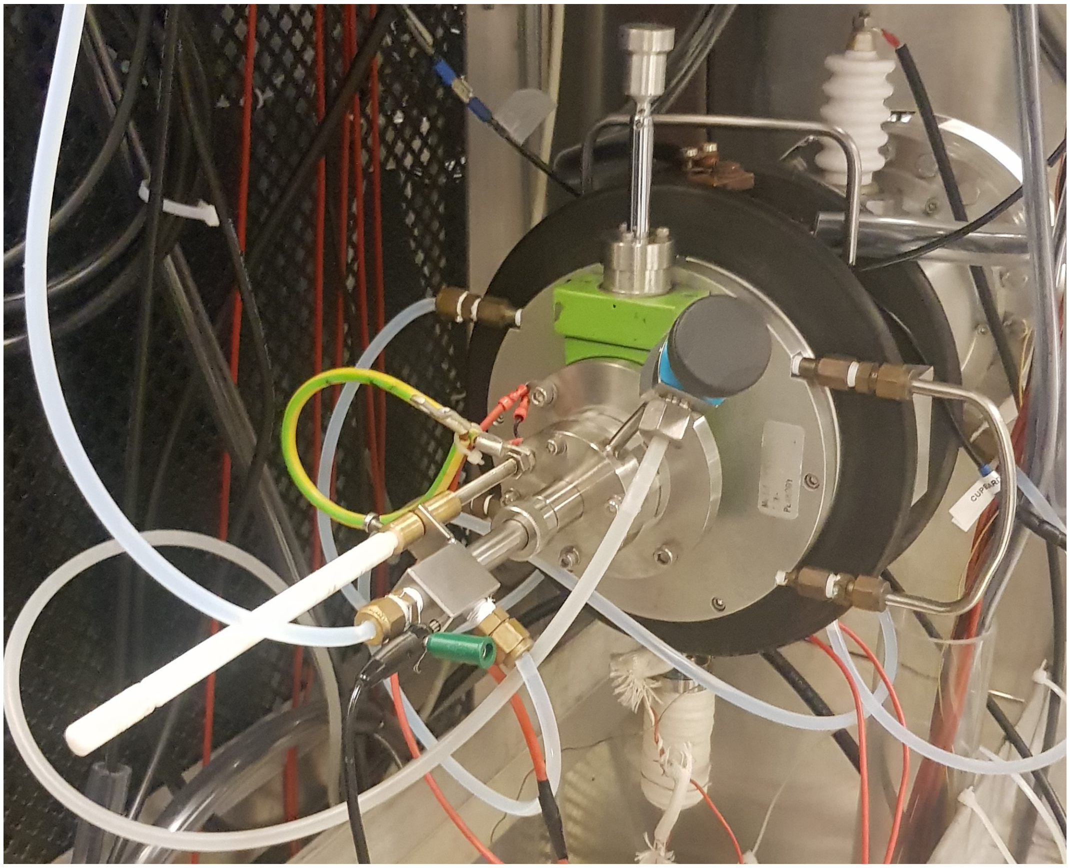

Figure 41: *Source exterior*

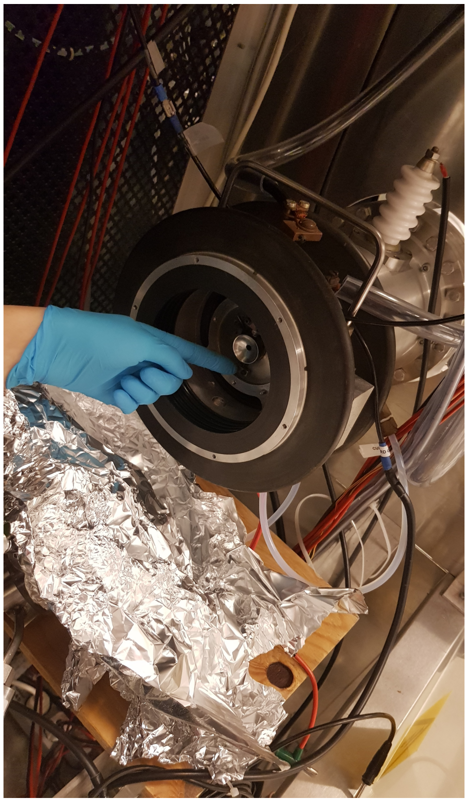

Figure 42: *Ionizer inside source*

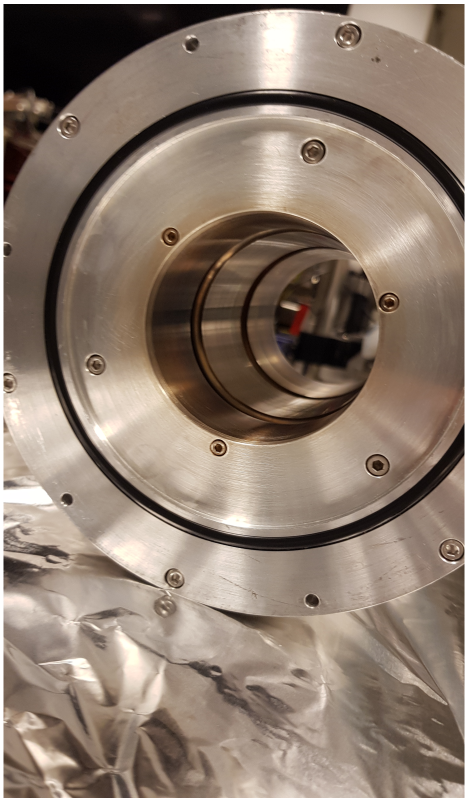

Figure 43: *Einzel lens*

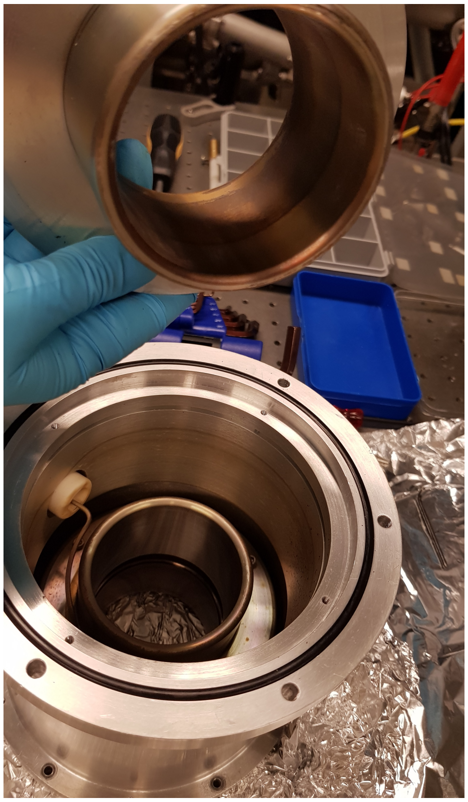

Figure 44: *Einzel lens*

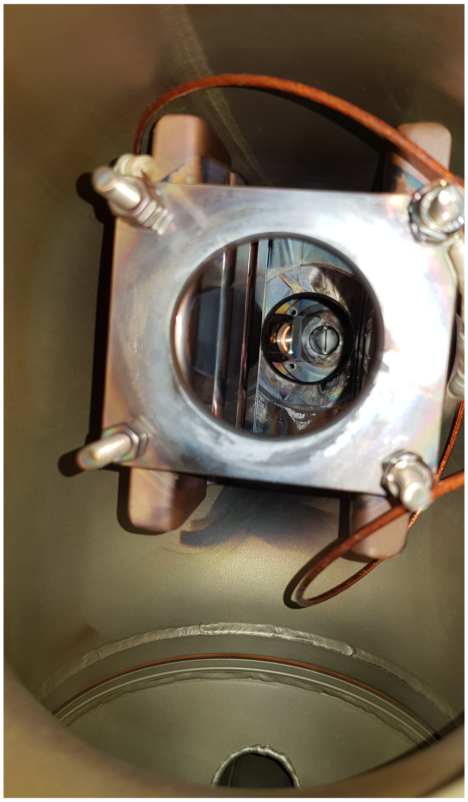

Figure 45: *X-lens*

Figure 46: *X-slit and mirror to monitor ionizer glow*

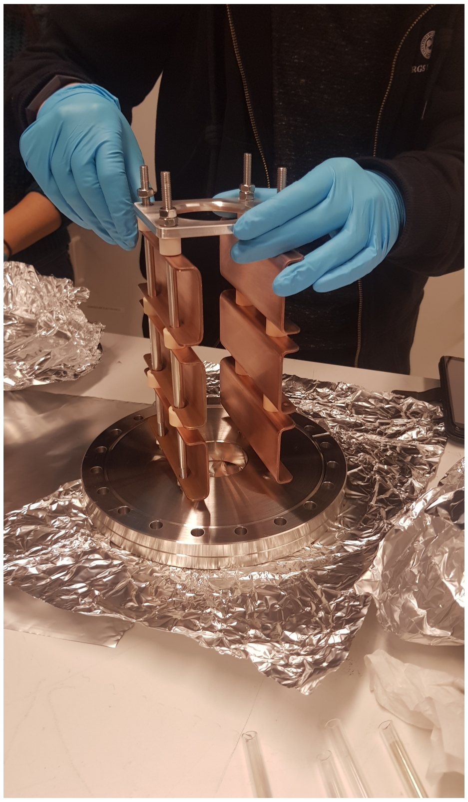

Figure 47: *Y-lens*

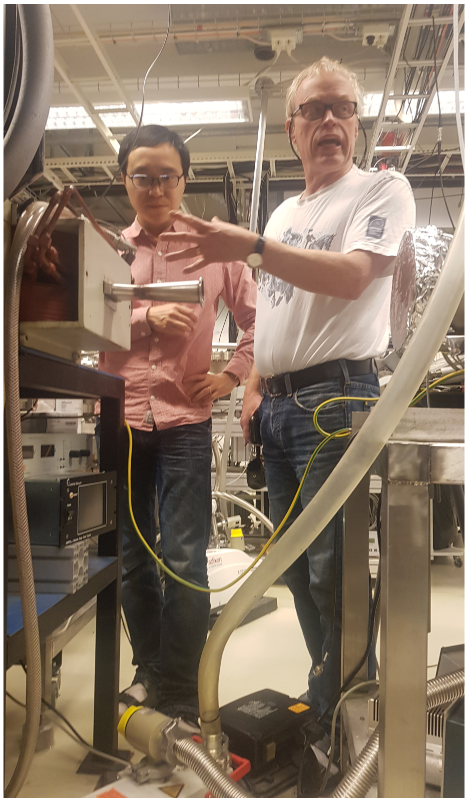

Figure 48: *Magnet discussion*

Figure 49: *Magnet tube welding*

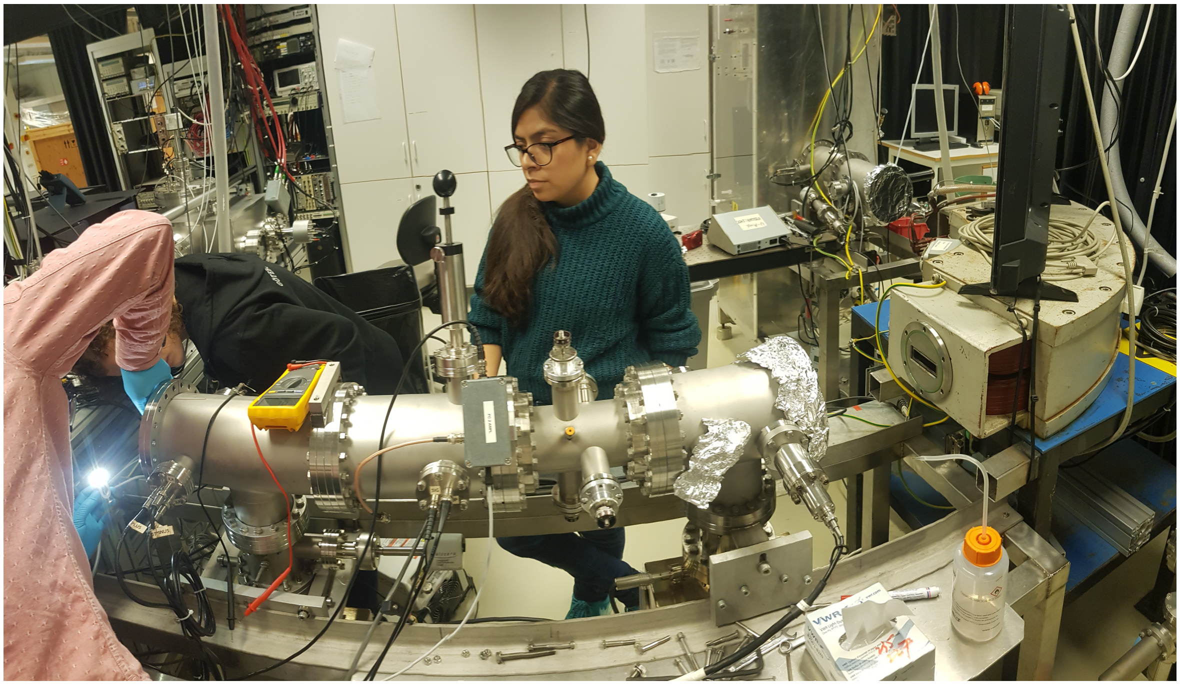

Figure 50: *Problem solving*

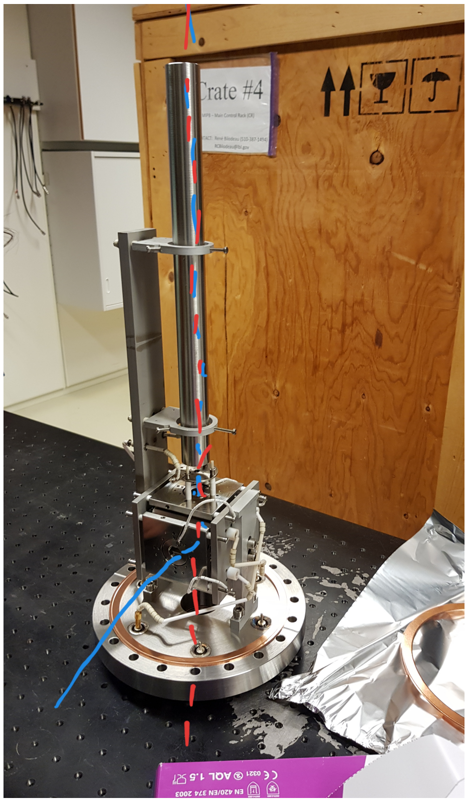

Figure 51: *Interaction region*

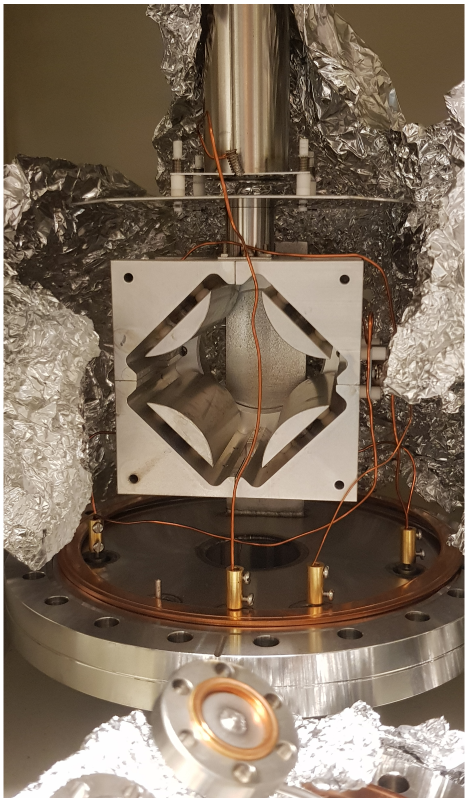

Figure 52: *Spare quadrupole deflector*

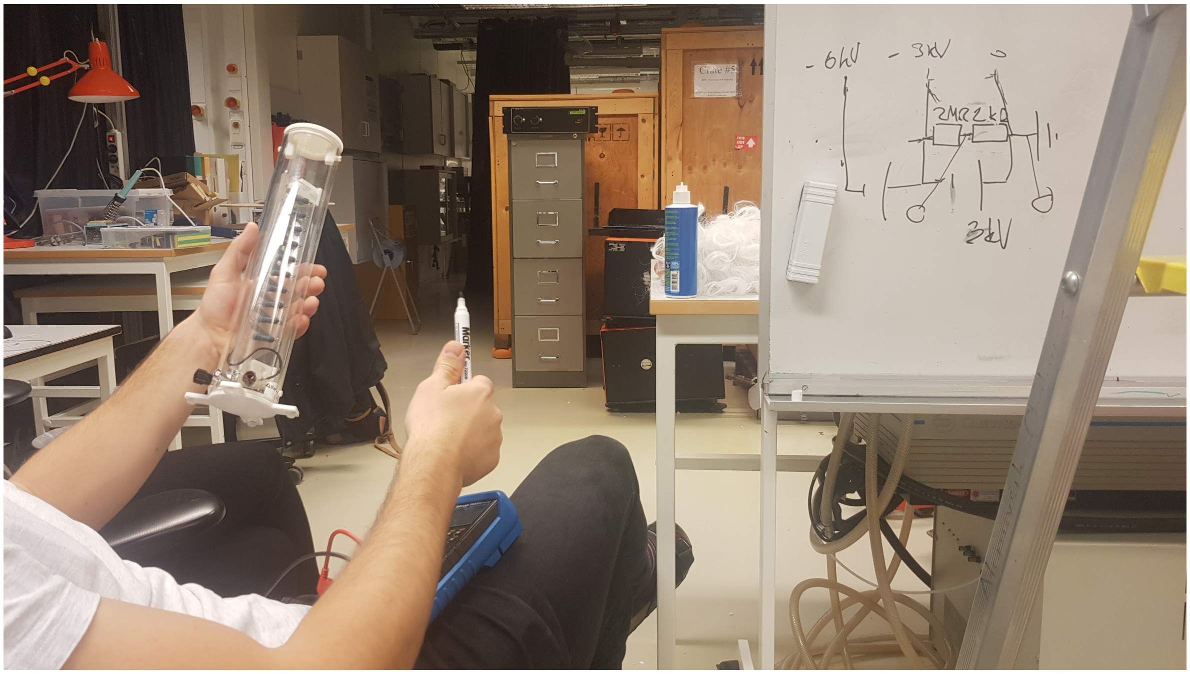

Figure 53: *Planning acceleration power supply test*

Figure 54: *Detector maintenance*

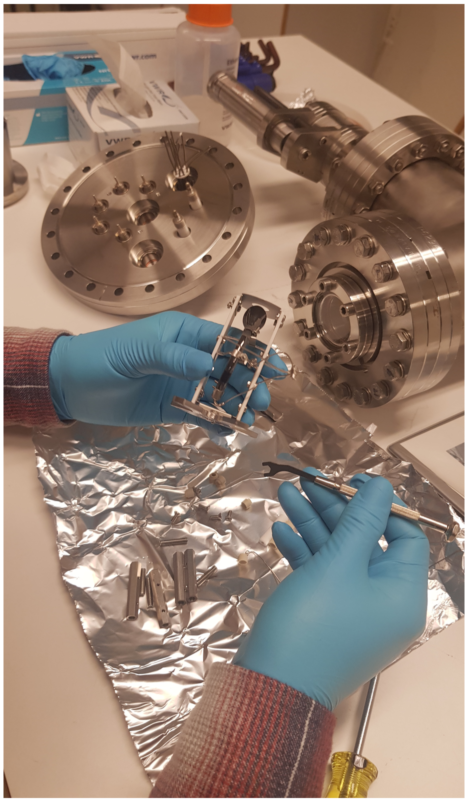

Figure 55: *Channeltron detector*

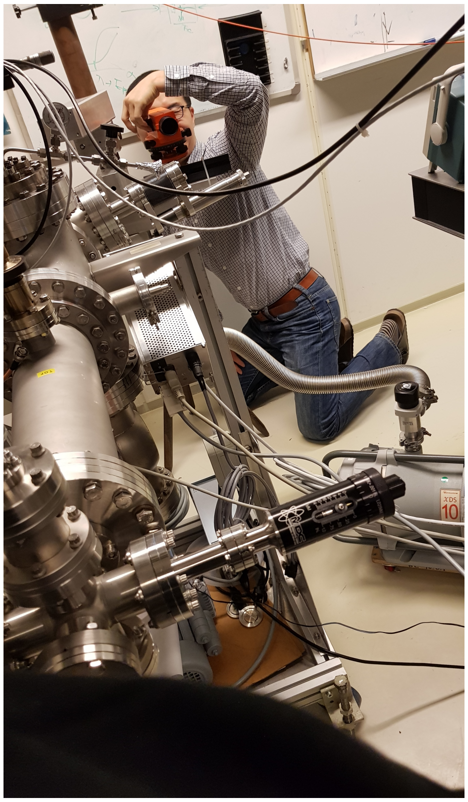

Figure 56: *Beamline alignment*

Figure 57: *Checking laser beam direction change (laser reflection tracking on postit) from cavity calibration*

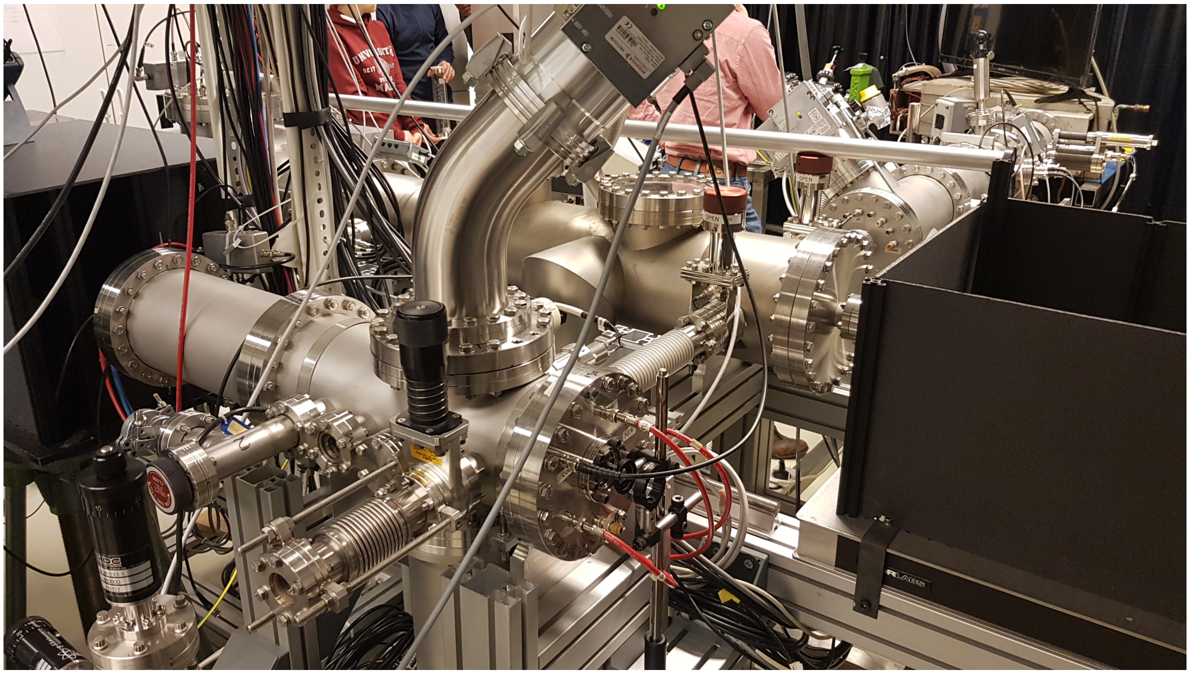

Figure 58: *Laser beam entrance into interaction region (after beamline alignment)*